



THE HONG KONG
POLYTECHNIC UNIVERSITY

香港理工大學

Pao Yue-kong Library

包玉剛圖書館

Copyright Undertaking

This thesis is protected by copyright, with all rights reserved.

By reading and using the thesis, the reader understands and agrees to the following terms:

1. The reader will abide by the rules and legal ordinances governing copyright regarding the use of the thesis.
2. The reader will use the thesis for the purpose of research or private study only and not for distribution or further reproduction or any other purpose.
3. The reader agrees to indemnify and hold the University harmless from and against any loss, damage, cost, liability or expenses arising from copyright infringement or unauthorized usage.

IMPORTANT

If you have reasons to believe that any materials in this thesis are deemed not suitable to be distributed in this form, or a copyright owner having difficulty with the material being included in our database, please contact lbsys@polyu.edu.hk providing details. The Library will look into your claim and consider taking remedial action upon receipt of the written requests.

**COPPER CHALCOGENIDES-BASED
THERMOELECTRIC MATERIAL FOR ENERGY
CONVERSION APPLICATION**

SHI DONGLIANG

PhD

The Hong Kong Polytechnic University

2019

The Hong Kong Polytechnic University

Department of Electrical Engineering

**Copper Chalcogenides-based Thermoelectric Material for Energy Conversion
Application**

SHI DONGLIANG

A thesis

submitted in partial fulfillment of the requirements

for the degree of

Doctor of Philosophy

May 2019

Certificate of Originality

I hereby declare that this thesis is my own work and that, to the best of my knowledge and belief, it reproduces no material previously published or written, nor material that has been accepted for the award of any other degree or diploma, except where due acknowledgment has been made in the text.

_____ (signed)

SHI DONGLIANG (Name of student)

14/05/2019 (Date)

Acknowledgments

The first and greatest acknowledgment is to my supervisor Dr. Kwok-ho Lam for over five years. Without him, this work would be impossible to achieve.

I would like to thank my parents for giving the endless support mentally, and their accompany throughout the whole Ph.D. period.

I own many thanks to the group members, Dr. Baojun Liu, Dr. Lu Shi, Mr. Zhi Ming Geng, Miss Ying Li, and Mr. Qi Zhang, for helping me to find my way during my first two years; especially to Zhi Ming for his help in the completion of the data measurement, and to Ying for her kind help in the revision of my thesis.

Without the outgoing attachment, I would never own the opportunity to do exchange in the renowned thermoelectric group in the Northwestern University. I own many thanks to my advisor, Professor G. Jeffrey Snyder, for his support and insights.

Thanks to Dr. Ying Cai Zhu for discussions about the SPB model and potential projects, and Dr. Stephen Dong Ming Kang for his instructive suggestions.

Abstract

The superionic thermoelectric material, copper selenide (Cu_{2-x}Se) has gained great attention due to its liquid-like behavior at high temperature. The liquid-like property could highly suppress the lattice thermal conductivity owing to the high mobility of Cu while maintain an excellent electrical conductivity, resulting in the large enhancement of thermoelectric efficiency. However, the high mobility of Cu also has some issues relating to thermal stability and data repeatability during thermal cycling tests, which is under great concern in recent years. Up to now, seldom reported articles systematically studied the data repeatability and the factors affecting the data repeatability and thermal stability. In this study, the Cu vacancy and selenium (Se) vacancy were studied using a conventional sintering method. Besides, the isothermal condition was also explored to suppress the evaporation of Se during the sintering progress. Finally, the parameters for the fabrication of Cu_{2-x}Se were determined, and the enhancement of thermoelectric efficiency was further studied by alloying with indium, In.

Cu_{2-x}Se ($x = 0.01, 0.03, 0.06$), superionic thermoelectric material (denoted as $\text{Cu}_{\text{vac-1}}$, $\text{Cu}_{\text{vac-3}}$, $\text{Cu}_{\text{vac-6}}$) was studied systematically by employing the conventional sintering method for the first time with regards to the phase structure, thermal stability, data repeatability and doping effect as well. The data repeatability of the Cu/Se system at heating and cooling cycling have been studied accordingly. It was found that the Cu vacancy strongly affects the data repeatability of the thermoelectric performance for the conventional sintered samples. Finally, the $\text{Cu}_{1.97}\text{Se}$ sample can have the excellent zT performance of 0.8 at 800 K with good repeatable data and cycling performance

To explore the effect of sintering temperature on the thermoelectric performance and data repeatability, the $\text{Cu}_{\text{vac-3}}$ sample was sintered at 873 K, 973 K, and 1073 K for 2 hours using the conventional sintering method. It was found that the sintering temperature could reach as low as 873 K to obtain a densified sample with good data repeatability in thermal cycling. However, the thermoelectric performance is relatively poor when compared to the ones sintered at 973 K and 1073 K. In the thermogravimetric analysis (TGA) analysis for the $\text{Cu}_{\text{vac-3}}$ powder, the evaporation of Se occurs at around 750 K, which is even slightly lower than the lowest sintering temperature adopted in the study. This means that the sample sintered at 873 K might also have the composition deviation with regard to the nominal composition.

To minimize the evaporation of selenium (Se) during the high-temperature sintering process, the vapor control and isothermal control were conducted during the conventional sintering process. The control experiment was conducted between the $\text{Cu}_{\text{vac-3}}$ sample sintered in a conventional tube furnace with the temperature gradient along the sintering chamber, and the sample sintered in a sealed small quartz tube located in the isothermal area of the tube furnace ($\text{Cu}_{\text{vac-3A}}$). By comparing the thermoelectric performance between these two samples, the conclusion can be made that the Cu-Se materials experience the severe evaporation of Se during the sintering process. The evaporation process is strongly related to the sintering temperature and the isothermal environment. The results provide the valuable information for the selection of spark plasma sintering (SPS) or hot press sintering (HPS) method to fabricate the Cu_2Se material.

To further enhance the thermoelectric performance, indium (In) is chosen as the dopant of $\text{Cu}_{\text{vac-3A}}$. With the introduction of In, the electrical conductivity, σ , of the doped $\text{Cu}_{\text{vac-3A}}$ is reduced, which is probably due to the reduced carrier concentration, n . It is found that the In-Cu-Se system is uncommon compared to the other dopants due to the partial solubility of In into the

Cu-Se system. The In dopant acts as a softening agent, which reduces the specific heat capacity, c_p , and the total thermal conductivity, κ_{tot} , of the sample due to the impurity phase of CuInSe₂. After applying the single parabolic model (SPB) model, the lattice thermal conductivity, κ_l , was found to be greatly reduced. The κ_l values of the Cu_{1.97}In_{0.03}Se sample (Cu_{vac}-3A-In) with the micron grain size are even lower than those of the samples with the nano grains. With the optimized doping amount of In, the zT of Cu_{vac}-3A-In approached 1 at 800 K. The SPB model predicts the optimized zT for Cu_{2-x}In_xSe that could reach to 1.8 at 800 K if n could be further reduced.

Table of Contents

Certificate of Originality	ii
Acknowledgments	iii
Abstract	iv
List of Figures	x
List of Tables	xvi
List of symbols	xvii
Chapter 1	
Introduction	
1.1 Thermoelectric Material and Thermoelectric Efficiency	1
1.2 Superionic Thermoelectric Material	2
1.3 Common Fabrication Methods for Superionic Thermoelectric Materials	5
1.4 Summary of the Research	7
Chapter 2	
Experimental Methods	
2.1 Materials Synthesis Methods	10
2.1.1 Conventional Sintering Method	10

2.2	Measurement of Transport Properties	10
2.2.1	Seebeck Coefficient and Electrical Conductivity Measurements	10
2.2.2	Thermal Conductivity Measurement	11
2.2.3	Hall Coefficient Measurement	12

Chapter 3

Thermoelectric Charge Transport Modeling

3.1	Boltzmann Transport Equation	15
3.2	Single Parabolic Band Model	18
3.3	Quality Factor	25

Chapter 4

Thermal Performance and Modeling for Cu_{2-x}Se Fabricated Using the Conventional Sintering Method

4.1	Materials Preparation	28
4.2	Results and Discussion	29
4.2.1	Microstructural Properties	29
4.2.2	Thermoelectric Performance	31
4.3	Conclusion	37

Chapter 5

Cycling Performance Study of $\text{Cu}_{1.97}\text{Se}$ Superionic Thermoelectric Material

5.1	Materials Preparation	38
5.2	Results and Discussion	39
5.2.1	Microstructural Properties	39
5.2.2	Thermoelectric Performance	44
5.3	Conclusion	50

Chapter 6

Vapor Pressure Control of the Conventional Sintering Method in the Fabrication of $\text{Cu}_{1.97}\text{Se}$ Superionic Thermoelectric Material

6.1.1	Materials Preparation	51
6.2	Results and Discussion	52
6.2.1	Microstructural Properties	53
6.2.2	Thermoelectric Performance	57
6.3	Conclusion	60

Chapter 7

Stoichiometric $\text{Cu}_{1.97}\text{In}_x\text{Se}$ Fabricated Using the Conventional Sintering Method

7.1	Materials Preparation	62
7.2	Results and Discussion	63
7.2.1	Microstructural Properties	63
7.2.2	Thermoelectric Performance	66

7.3	Conclusion	70
-----	------------	----

Chapter 8

	Future Work	72
--	-------------	----

	Bibliography	74
--	--------------	----

List of Figure Captions

	Page
Figure 1.1	High-temperature phase structure of Cu_2Se (Green color stands for the Se atom, and blue-white color stands for the Cu atom). 3
Figure 1.2	(a) A photo of the surface of Cu_2S pellet fabricated using the SPS method, (b) a photo of the cross-section of the Cu_2S sample (G. Dennler et al., 2014). 4
Figure 1.3	From left to right: Cu_2Se sample after current stress of 24 A cm^{-2} for 24 h, $\text{Cu}_{1.8}\text{S}$ and CuS samples after current stress of 48 A cm^{-2} for 72 h, respectively (G. Dennler et al., 2014). 4
Figure 1.4	Structure setup of an SPS sintering method for thermoelectric material (F. Kaiser et al., 2017). 6
Figure 2.1	Van der Pauw approach for the measurements of (a) ρ and (b) R_H (Elton et al., 2003). 12
Figure 3.1	The μ_H curve as a function of temperature plotted in a log-log format by using the SPB model, assuming the interaction of phonons and electrons are mainly due to the acoustic phonon scattering at medium and high temperatures. 22
Figure 3.2	Room-temperature μ_H curve as a function of n_H . The parameters at 300 K and 350 K are represented by a solid line and a dashed line, respectively. $m_d^* = 1.86m_e$, $C_{11} = 116.3 - 0.0208T$ ($300 \text{ K} < T < 900 \text{ K}$), $E_{def} = 8.3 \text{ eV}$. 23

Figure 3.3.	The absolute value of the room-temperature S calculated by the SPB model.	24
Figure 3.4	zT vs η with different B of the thermoelectric material.	26
Figure 4.1	Heating treatment process for Cu_{2-x}Se . (a) Heat treatment for ingot synthesis with cooling inside the furnace to room temperature, (b) heat treatment for bulk samples synthesis at different sintering temperatures for 2 hours with the controlled cooling rate.	29
Figure 4.2	Powder X-ray diffraction (PXRD) patterns measured at room temperature for (a) $\text{Cu}_{1.94}\text{Se}$ ($\text{Cu}_{\text{vac-6}}$) sintered at 973 K. (Black column bars show the standard PDF card #47-1448 diffraction peak sites for the orthorhombic Cu_2Se_x phase and PDF card #06-0680 diffraction peak sites for the high-temperature cubic phase Cu_{2-x}Se), (b) $\text{Cu}_{1.97}\text{Se}$ ($\text{Cu}_{\text{vac-3}}$) sintered at 973 K. (Black column bars show the standard PDF card #27-1131 diffraction peak sites for the low-temperature monoclinic Cu_2Se phase), (c) $\text{Cu}_{1.99}\text{Se}$ ($\text{Cu}_{\text{vac-1}}$) sintered at 973K. (Black column bars show the standard PDF card #47-1448 diffraction peak sites for the low-temperature Monoclinic Cu_2Se phase)	30
Figure 4.3	SEM images for the cross-sections of the as-sintered (a) $\text{Cu}_{\text{vac-6}}$, (b) $\text{Cu}_{\text{vac-3}}$, and (c) $\text{Cu}_{\text{vac-1}}$.	31
Figure 4.4	Temperature dependence of (a) σ , (b) S and (c) PF for Cu_{2-x}Se sintered at 973 K for 2 hours.	32
Figure 4.5	Temperature dependence of (a) D , and (b) κ_{tot} for Cu_{2-x}Se .	33
Figure 4.6	Temperature dependence of (a) L_0 of Cu_{2-x}Se derived and the metallic	34

limit represented by the dashed line, and (b) κ_e derived by using the equation $\kappa_e = L_0\sigma T$.

- Figure 4.7 Temperature dependence of U for Cu_{2-x}Se evaluated by the S and σ measured at one single temperature. 35
- Figure 4.8 Temperature dependence of σ_E of Cu_{2-x}Se . 36
- Figure 4.9 Hall carrier concentration, n_p and mobility, μ as a function of Cu vacancy content x at room temperature 37
- Figure 4.10 (a) Temperature dependence of zT for Cu_{2-x}Se with different Cu vacancies (dashed line represents the theoretical curve of Cu_2Se), and (b) SPB model results at 800 K (black dash line for zT and red dashed line for S) with the measured zT of $\text{Cu}_{\text{vac-3}}$ (represented by a star symbol). 38
- Figure 5.1 TGA curves for (a) the $\text{Cu}_{\text{vac-3}}$ powder obtained from the melt ingot, and (b) the $\text{Cu}_{\text{vac-3}}$ powder under different heating rates. 41
- Figure 5.2 PXRD patterns for $\text{Cu}_{\text{vac-3}}$ sintered at 873 K, 973 K, and 1073 K for 2 hours. (Black column bars show the monoclinic Cu_2Se phase (standard PDF card #27-1131)) 42
- Figure 5.3 Rietveld refinements of XRD profiles of $\text{Cu}_{\text{vac-3}}$ sintered at different temperatures: (a) 873 K, (b) 973 K and (c) 1073 K. 44
- Figure 5.4 SEM images for the cross-sections of $\text{Cu}_{\text{vac-3}}$ sintered with different temperatures: (a) 873 K, (b) 973 K and (c) 1073 K. 45
- Figure 5.5 Temperature dependence of (a) σ , (b) S and (c) PF for $\text{Cu}_{\text{vac-3}}$ sintered at different temperatures. 47

- Figure 5.6 Thermal cycling performance for $\text{Cu}_{\text{vac-3}}$ sintered at 1073 K: (a) σ , (b) S and (c) PF . 48
- Figure 5.7 Thermal cycling performance for $\text{Cu}_{\text{vac-3}}$ sintered at 1073 K: (a) σ , (b) S and (c) PF . 49
- Figure 5.8 Temperature dependence of (a) κ_e and (b) κ_l for $\text{Cu}_{\text{vac-3}}$ sintered at different temperatures. 50
- Figure 5.9 (a) Temperature dependence of zT of $\text{Cu}_{\text{vac-3}}$ sintered at different temperatures, and (b) SPB model results at 800 K with the measured zT of $\text{Cu}_{\text{vac-3}}$ sintered at different temperatures (represented by solid symbols with the colors corresponding to the curves). 51
- Figure 6.1 The sintering setups for samples in a conventional tube furnace with an isothermal space marked by a red square: (a) samples placed in the isothermal space and exposed to the sintering atmosphere, and (b) samples sealed in a small quartz tube located in the isothermal space (the length of a small quartz tube is within the isothermal space of the tube furnace). 54
- Figure 6.2 PXRD patterns for $\text{Cu}_{\text{vac-3}}$ sintered at 873 K in a tube furnace. The data was collected from 323 K to 473 K per 50 K in vacuum. (Blue column bars show the standard PDF card #27-1131 diffraction peak sites for the low-temperature α - Cu_2Se phase; Red column bars show the standard PDF card #46-1129 diffraction peak sites for the high-temperature β - Cu_2Se phase). 55
- Figure 6.3 TGA curves for weight losses of the $\text{Cu}_{\text{vac-3}}$ powder from ingot (red line), 56

- the Cu_{vac}-3 (blue line) and Cu_{vac}-3A (purple line) bulk samples.
- Figure 6.4 Rietveld refinement results of the high-temperature PXRD by using GSAS software. 57
- Figure 6.5 High-temperature PXRD patterns for Cu_{vac}-3 sintered at 873 K and 1073 K in a tube furnace and Cu_{vac}-3A sintered at 973K. The black column bars show the standard PDF card #46-1129 diffraction peak sites for the high-temperature β -Cu₂Se phase. 58
- Figure 6.6 SEM image for the cross-sections of Cu_{vac}-3A. 59
- Figure 6.7 Temperature dependence of (a) σ , (b) S , and (c) PF for Cu_{vac}-3 and Cu_{vac}-3A, respectively. 60
- Figure 6.8 Temperature dependence of (a) D , and (b) κ_{tot} for Cu_{vac}-3 and Cu_{vac}-3A sintered at 973 K. 61
- Figure 6.9 Temperature dependence of (a) κ_e , and (b) κ_l for Cu_{vac}-3 and Cu_{vac}-3A sintered at 973 K. 61
- Figure 6.10 (a) Temperature dependence of zT for Cu_{vac}-3 and Cu_{vac}-3A sintered at 973 K, and (b) SPB model results at 800 K (black dash line for zT and red dashed line for S) with the measured zT of Cu_{vac}-3A (represented by a square symbol). 62
- Figure 7.1 PXRD patterns for Cu_{vac}-3A-In at room temperature and 473 K. 66
- Figure 7.2 Rietveld refinements of high-temperature PXRD profiles of (a) Cu_{vac}-3A and (b) Cu_{vac}-3A-In using GSAS software. 66

- Figure 7.3 TGA data for weight losses of the $\text{Cu}_{\text{vac}}\text{-3}$ powder from ingot (red line), the $\text{Cu}_{\text{vac}}\text{-3A}$ (blue line) and $\text{Cu}_{\text{vac}}\text{-3A-In}$ (green line) bulk samples. 67
- Figure 7.4 SEM image for the cross sections of $\text{Cu}_{\text{vac}}\text{-3A-In}$, and (inset) the picture of the as-prepared ingot. 68
- Figure 7.5 Temperature dependence of (a) σ , (b) S and (c) PF for $\text{Cu}_{\text{vac}}\text{-3A-In}$ and $\text{Cu}_{\text{vac}}\text{-3A}$. 69
- Figure 7.6 Temperature dependence of the specific heat capacity, c_p , for $\text{Cu}_{\text{vac}}\text{-1}$, $\text{Cu}_{\text{vac}}\text{-3A}$ and $\text{Cu}_{\text{vac}}\text{-3A-In}$ 70
- Figure 7.7 Temperature dependence of (a) D and (b) κ_{tot} for $\text{Cu}_{\text{vac}}\text{-3A}$ and doped $\text{Cu}_{\text{vac}}\text{-3A-In}$. 72
- Figure 7.8 Temperature dependence of calculated (a) κ_e , and (b) κ_l for $\text{Cu}_{\text{vac}}\text{-3A}$ and In-doped $\text{Cu}_{\text{vac}}\text{-3A-In}$. 72
- Figure 7.9 (a) Temperature dependence of zT for $\text{Cu}_{\text{vac}}\text{-3A}$ and $\text{Cu}_{\text{vac}}\text{-3A-In}$, and (b) SPB model results at 800 K (black dash line for zT and red dashed line for S) with the measured zT of $\text{Cu}_{\text{vac}}\text{-3A-In}$ (represented by a circle symbol). 73

List of Tables

	Page
Table 5.1 Rietveld analysis of the XRD results for Cu _{vac} -3.	44
Table 6.1. Lattice parameters derived from the XRD patterns for Cu _{vac} -3 sintered at 873 K and 1073 K, and Cu _{vac} -3A.	59
Table 7.1. Rietveld analysis of PXRD results for Cu _{vac} -3A and Cu _{vac} -3A-In.	66

List of symbols

zT , Figure of merit

S , Seebeck coefficient

σ , Electrical conductivity

κ_{tot} , Total thermal conductivity

T , Temperature

V , Thermoelectric voltage

α_A , Slope of the V-T plot related to the measurement using the n-type probe

α_B , Slopes of the V-T plot related to the measurement using the p-type probe

S_{AB} , the contact potential difference of thermocouple

S_A , Thermoelectric voltage for the n-type thermocouple

S_B , Thermoelectric voltage for the p-type thermocouple

D , Thermal diffusivity

d , Geometric density

c_p , Specific heat capacity at constant pressure

R_H , Hall coefficient

n_H , Hall carrier concentration

μ_H , Hall mobility factor

ρ , Resistivity

r_H , Hall factor

B_{mag} , Magnetic field strength

d_{thick} , Sample thickness

f_{cor} , Correction factor

I_{21} , Current from probe 2 to 1

V_{34} , Voltage between 3 and 4

$R_{34,21}$, Resistance measured with current through probe 2 to 1 and voltage between probe 3 and 4

V_H , Hall voltage

t , Time

x , Position

p , Momentum

f , Distribution function

f_0 , Unperturbed distribution function

\hbar , Reduced Planck constant

k , Wave vector

τ , Electron relaxation time

E_{ext} , External electric field

E_F , Fermi energy or Fermi level

F , Force

m , Mass

$f_F(E)$, Fermi-Dirac distribution function

E , Energy

ψ , A function parameter for zT calculation

ε , Chemical potential

ϵ , Reduced chemical potential

η , Reduced electrochemical potential

v , Velocity

k_B , Boltzman constant

E_{tot} , Total electric field

q_e , Electric charge

e , Euler's number

τ_{const} , Electron relaxation time factor

r , Scattering parameter

E^* , Reduced energy

E_F^* , reduced Fermi energy

$g(E)$, density of state function

N_v , number of bands

m_d^* , density-of-state effective mass

m_x , the principal effective masses in the x-direction

m_y , the principal effective masses in the y-direction

m_z , the principal effective masses in the z-directions

n , electron concentration

F_s , Fermi integral

j , current density

v_x , velocity in the x-direction

μ , electron mobility

μ_0 , mobility parameter

C_{11} , the elastic constant for longitudinal vibrations

E_{def} , deformation potential

m_c^* , the conductive effective mass

L_0 , Lorenz number

κ_l , lattice thermal conductivity

κ_e , electronic contribution to total thermal conductivity

v_l , longitudinal velocity

v_t , transverse velocity

κ_{lmin} . Minimum lattice thermal conductivity

V_{vol} , atomic volume

σ_{E_0} , transport coefficient

B , quality factor

$\frac{m^*}{m_e}$, relative effective mass

PF , power factor

List of Publications

Geng, Zhiming[^], Shi, Dongliang[^], Shi, Lu, Li, Ying, Snyder, G. Jeffrey, **Lam, Kwok Ho***. “Conventional sintered Cu_{2-x}Se thermoelectric material”. *Journal of Materiomics* (online published)

Shi, Dongliang, Geng, Zhiming, **Lam, Kwok Ho***. “Study of conventional sintered Cu_2Se thermoelectric material”. *Energies*, Vol.12, 401 (2019)

Lin, Bo, Pan, Li-Hong, Shi, Dong-Liang, Huang, Hua-Kun, He, Fuan, **Lam, Kwok-ho*** and Wu, Hui-Jun. “Preparation and characterization of composites based on poly(vinylidene fluoride-co-chlorotrifluoroethylene) and carbon nanofillers: a comparative study of exfoliated graphite nanoplates and multi-walled carbon nanotubes”. *Journal of Materials Science*, Vol.54, pp.2256–2270 (2019)

Yang, Ying, Chen, Junjun, Li, Ying, Shi, Dongliang, Lin, Bo, Zhang, Shijie, Tang, Yiwen, He, Fuan*, **Lam, Kwok Ho*** “Preparation and dielectric properties of composites based on PVDF and PVDF-grafted graphene obtained from electrospinning-hot pressing method”. *Journal of Macromolecular Science, Part A: Pure and Applied Chemistry*, Vol.55, 148–153 (2018)

Suen, Chun Hung[^], Shi, Dongliang[^], Su, Y, Zhang, Zhi, Chan, Cheuk Ho, Tang, Xiaodan, Li, Y, **Lam, Kwok-ho***, Chen Xinxin, Huang, B.L., Zhou, X.Y. and Dai, Ji-yan*. "Enhanced thermoelectric properties of SnSe thin films grown by pulsed laser glancing-angle deposition". *Journal of Materiomics*, Vol.3, pp.293–298 (2017)

Shi, Dongliang, Zhang, Qi, Ye, Yuan Mao, Luo, Lingling, Cheng, Eric Ka-wai, Lin, Dunmin* and **Lam, Kwok-ho***. “High-frequency current sensor based on lead-free multiferroic BiFeO_3 - BaTiO_3 -based ceramics". *Measurement*, Vol.104, pp.287–293 (2017)

Chapter 1

Introduction

1.1 Thermoelectric Material and Thermoelectric Efficiency

With the increasing consumption of fossil fuels, environmental issues have drawn much more attention and led to the application of novel green energy materials. The thermoelectric material is a promising solid-state material that can convert energy between heat and electricity (G. J. Snyder et al., 2008; S. N. Girard et al., 2011). Its merit includes being compact in size, silent and with no tangible moving parts.

Nevertheless, the applications are still constrained by the low efficiency of thermoelectric materials particularly when compared to other renewable energy sources, leading to a bottleneck in the area of thermoelectric technology. A figure of merit, zT , has been defined to characterize the conversion efficiency that could be obtained from the specific thermoelectric material:

$$zT = \frac{S^2\sigma}{\kappa_{tot}}T \quad (1.1)$$

where S is the Seebeck coefficient, σ is the electrical conductivity, κ_{tot} is the total thermal conductivity, and T is the temperature of the thermoelectric material. Thus, pursuing high zT is amongst the hottest topics in thermoelectric materials research (A. A. Olvera et al., 2017; G. J. Snyder et al., 2008; B. Yu et al., 2012; F. Hergert et al., 2006; H. Chi et al., 2014; H. Kim et al., 2015; R. D. Heyding et al., 1976; M. Oliveria et al., 1988; A. L. N. Stevels et al., 1971; S. A. Danilkin et al., 2003; S. A. Danilkin et al., 2011; H. Liu et al., 2013; S. Ballikaya et al., 2013; D. R. Brown et al., 2013; H. L. Liu et al., 2013).

1.2 Superionic Thermoelectric Material

In recent years, the enhancement of thermoelectric performance has been implemented by various approaches, such as the formation of nano-inclusion structures (A. A. Olvera et al., 2017), phase boundary modification (J. J. Guo et al., 2018), the use of resonant level enhancement (L. Wu et al., 2017), increasing band degeneracy by promoting band convergence via the adjustment of temperature (Y. Pei et al., 2011) or composition (M. Wood et al., 2018). The aforementioned techniques have a common goal of modifying the electron transport of thermoelectric materials. Another approach is to develop the materials with strong phonon scattering, such as the materials with strong intrinsic anharmonicity (D. T. Morelli et al., 2008), the newly proposed phonon-liquid-electron crystal material (H. Liu et al., 2012; D. J. Voneshen et al., 2017), and the materials with the capability of suppressing transverse phonons while retaining effective electron transport.

Copper selenide, Cu_2Se , is one of the materials that exhibit the latter characteristics. The crystal structure of Cu_2Se undergoes a phase transition at ~ 414 K depending on the stoichiometric ratio of copper (Cu) to selenium (Se). The so-called superionic phase refers to the high-temperature phase of Cu_2Se as shown in Figure 1.1. The high-temperature superionic structure can be categorized as an antiferroite structure with space group $\text{Fm}\bar{3}\text{m}$. The Se ions occupy at the face-centered lattice. Besides, it is widely recognized that the randomly located Cu ions in the octahedral 4b sites, tetrahedral 8c sites, and trigonal 32f sites could provide relatively low κ_{tot} .

F. S. Liu et al. has reported the tin (Sn) doped Cu_2Se material fabricated using the spark plasma sintering (SPS) technique, which improved its zT to 1.4 at 823 K (F. S. Liu et al., 2015). L. Yang et al. also reported the nano-sized Cu_2Se with tellurium (Te) dopant. An average zT value of ~ 1.2 was observed for the $\text{Cu}_2\text{Se}_{0.98}\text{Te}_{0.02}$ sample fabricated using the SPS technique (L. Yang et al.,

2016). High-temperature thermoelectric properties of $\text{Cu}_{2-x}\text{Ag}_{0.03}\text{Se}_{1+y}$ have also been studied by using the hot press sintering (HPS) technique (T. W. Day et al., 2014). Adding silver (Ag) into Cu_2Se could increase the zT up to 1.0 at 870 K. Sajid Butt et al. reported Te-doped Cu_2Se with enhanced thermoelectric performance in the mid-temperature range (X. Zhang et al., 2015). The nanoscale Cu_2Te clusters were introduced in the parent phase by using the ball-milling method followed by the SPS technique. A large zT value of 1.9 could be reached for the $\text{Cu}_2\text{Se}_{0.9}\text{Te}_{0.1}$ sample (S. Ballikaya et al., 2013). S. Ballikaya et al. first investigated the Ag-doped overstoichiometric Cu_{2-x}Se by the SPS technique, reaching a zT value of ~ 0.52 at 650 K.

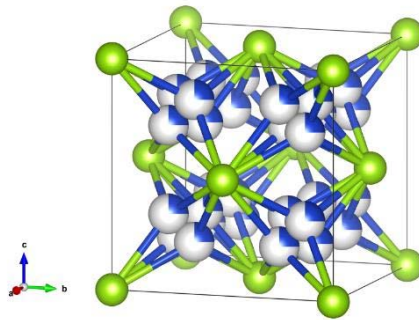


Figure 1.1 High-temperature phase structure of Cu_2Se (Green color stands for the Se atom, and blue-white color stands for the Cu atom).

Although Cu_2Se and copper sulfide (Cu_2S) have recently been proposed as promising thermoelectric materials due to its low-cost and environmental friendly merits, the study of these materials was started ~ 190 years ago. Despite the merits, these materials suffer from some critical intrinsic issues; thus, they have not been adopted for large-scale commercial and industrial utilization. The prime issue of these materials comes from the strong diffusion of Cu that leads to the limited efficiency and the reliability of thermoelectric devices. For example, when a large current is applied, precipitation of Cu takes place at the cathode side that was observed by Miyatani

and Ema for Cu_2S and Cu_2Se materials in 1960 and 1990, respectively (S. Y. Miyatani et al., 1953). Moreover, when the Cu_2Se sample was exposed to the high current density or high working temperature, the obvious weight loss (the evaporation of Se) was found by the General Atomics Corporation in the late 1970s (G. Stapfer et al., 1979). Other researchers also found the similar problem directly or observed the non-repeatable electrical properties at thermal cycles (G. Dennler et al., 2014; A. Bohra et al., 2016; T. P. Bailey et al., 2016). The migration of Cu to the surface of the testing sample can even be visible as shown in Figures 1.2 and 1.3 (G. Dennler et al., 2014).



Figure 1.2 (a) A photo of the surface of Cu_2S pellet fabricated using the SPS method, (b) a photo of the cross-section of the Cu_2S sample (G. Dennler et al., 2014).



Figure 1.3 From left to right: Cu_2Se sample after current stress of 24 A cm^{-2} for 24 h, $\text{Cu}_{1.8}\text{S}$ and CuS samples after current stress of 48 A cm^{-2} for 72 h, respectively (G. Dennler et al., 2014).

As observed in Figure 1.3, the appearance of Cu_2Se is entirely changed after the current stress test, which is quite different from the Cu and S binary system. It seems that $\text{Cu}_{1.8}\text{S}$ and CuS exhibit

better chemical stability that could withstand higher current density for longer operating time. To solve the issue of Cu precipitation on the surface of samples, various strategies have been proposed, such as the insertion of the baffled coatings to reduce the Se evaporation. Alternatively, the other approach is to internally change the chemical composition via the doping technique (D. R. Brown et al., 2013; R. Nunna et al., 2017; P. Qiu et al., 2014; T. P. Bailey et al., 2016).

T. P. Bailey et al. adopted a doping approach to chemically stabilize the Cu_2Se sample fabricated using the SPS technique. With the increasing dopant content of tin (Sn), the degradation was minimized at 773 K, and the testing current density could reach 12 A cm^{-2} (T. P. Beiley et al., 2016). A. A. Olvera et al. first introduced a hybrid structure into the high-temperature Cu_2Se phase, causing strong phonon scattering while maintaining excellent thermal stability. To maintain the nanosize of the grain, the hot press (fast sintering) technique is still a promising approach.

1.3 Common Fabrication Methods for Superionic Thermoelectric Materials

Regarding the fabrication of thermoelectric materials, various methods have been developed. Among them, the most widely used methods are SPS and HPS. The SPS technique is similar to the rapid sintering, which is extremely useful to obtain a highly densified sample and avoid the grain growth at high sintering temperatures. The typical structure of an SPS setup is shown in Figure 1.4.

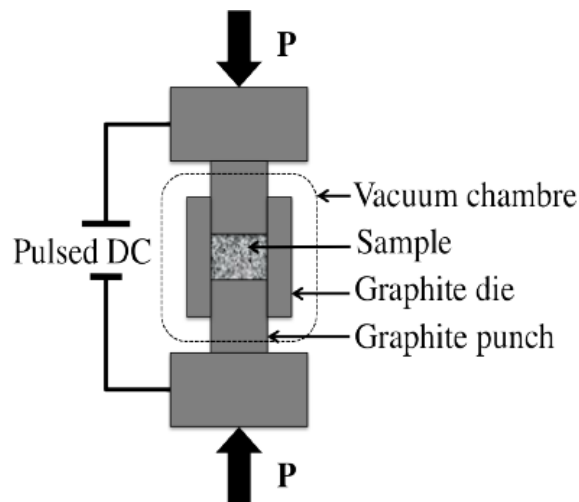


Figure 1.4 Structure setup of an SPS sintering method for the fabrication of thermoelectric materials (F. Kaiser et al., 2017).

For the superionic thermoelectric materials, SPS could induce the deviation of the nominal ratio and the non-uniform composition across the sample because of the Cu precipitation at the cathode side. This is typically the cause of the unstable performance of the superionic thermoelectric samples in high temperatures.

The SPS technique features a very high heating or cooling rate (up to 1000 K/min) due to the internal heat generation (D. R. Brown et al., 2013). The possible solution for the migration of Cu in the Cu-Se/S materials is to use the external heat source, which refers to another popular sintering technique: HPS technique (S. D. Kang et al., 2017). The structure of the HPS setup is similar to the SPS one, except the heat source. The external heat transfer to the sample may avoid the migration of Cu under the strong electric field. Taking this into account, the HPS method is more favorable for the study of superionic materials. However, the HPS technique needs a die that can withstand the high operating temperature. A graphite paper is used as a liner separator of graphite die to isolate the powder from the die. If the powders are active metals such as alkalis or an alkaline

earth metal, the HPS method cannot be used due to the reactivity between the graphite and active metals. Consequently, other approaches may be required, such as the conventional sintering method.

The conventional sintering method has widely been used in the ceramics industry because of its simplicity in adoption and high cost-effectiveness. However, there are few reported papers related to the thermoelectric materials fabricated using the conventional sintering method. This may be due to the relative slow sintering process that may not give highly densified thermoelectric samples with good mechanical strength. Nevertheless, it is still worth investigating the feasibility of using the conventional sintering method to develop thermoelectric materials especially for those with strong metallic bond materials due to their good sintering ability. Besides, this method is also good for large-scale industrial use because of the high cost-effective characteristics.

1.4 Summary of the Research

1.4.1 Study of the Base Material

Cu_{2-x}Se ($x = 0.01, 0.03, 0.06$) is the main base material for this research. The sintering condition for the conventional sintering method is chosen at 973 K with a dwelling time of 2 hours. Firstly, the undoped Cu_{2-x}Se fabricated using the conventional sintering method is explored systematically regarding to different Cu vacancy densities. Due to the feasibility of changing the carrier concentration, the thermoelectric performance can be highly associated with the Cu vacancy according to the results. Besides, the data repeatability of the Cu/Se system at heating and cooling cycling are all studied accordingly. It is found that the Cu vacancy strongly affects the data repeatability of the thermoelectric performance for the conventional sintered sample.

According to the results, the $\text{Cu}_{1.97}\text{Se}$ sample, denoted as $\text{Cu}_{\text{vac-3}}$, can have the excellent repeatable data and cycling performance. Thus, this composition was taken as the study subject to explore the influence of the sintering temperature to the thermoelectric performance. Meanwhile, the other critical concern is to optimize the sintering temperature.

To explore the effect of sintering temperature on the thermoelectric performance and data repeatability, the $\text{Cu}_{\text{vac-3}}$ sample was sintered at 873 K, 973 K, and 1073 K for 2 hours using the conventional sintering method. The major work for this experimental design is to investigate the relationship between the sintering temperature and thermoelectric performance. It is found that the sintering temperature could reach as low as 873 K to obtain a densified sample with good cycling repeatability. However, the thermoelectric performance is relatively low when compared to the ones sintered at 973 K and 1073 K. In the thermogravimetric analysis (TGA) analysis for the $\text{Cu}_{\text{vac-3}}$ powder, the evaporation of Se occurs at around 750 K, which is even slightly higher than the lowest sintering temperature adopted in the study. This means that the sample sintered at 873 K might also have the composition deviation with regard to the nominal composition.

To minimize the evaporation of Se during the high-temperature sintering process, the specified experiment is designed. The comparative experiment was conducted between the $\text{Cu}_{\text{vac-3}}$ sample sintered in a conventional tube furnace with the temperature gradient along the sintering chamber, and the sample sintered in a sealed small quartz tube located in the isothermal area of the tube furnace ($\text{Cu}_{\text{vac-3A}}$). By comparing the thermoelectric performance between these two samples, the conclusion can be made that the Cu-Se materials experience the severe evaporation of Se during the sintering progress. The evaporation progress is strongly related to the sintering temperature and the isothermal environment. These research results also provide valuable information for the selection of SPS or HPS method as the fabrication of Cu_2Se material.

To further enhance the thermoelectric performance, indium (In) is chosen as the dopant of $\text{Cu}_{\text{vac}}\text{-3A}$. With the introduction of In, the σ of the doped $\text{Cu}_{\text{vac}}\text{-3A}$ is reduced, which is probably due to the reduced carrier concentration, n . It is found that the In-Cu-Se system is uncommon compared to the other dopants due to the partial solubility of In into the Cu-Se system. The In dopant acts as a softening agent, which reduces the specific heat capacity, c_p , and κ_{tot} of the sample due to the impurity phase of CuInSe_2 . After applying the single parabolic model (SPB) model, the lattice thermal conductivity, κ_l , is found to be greatly reduced. The κ_l values of the $\text{Cu}_{1.97}\text{In}_{0.03}\text{Se}$ sample ($\text{Cu}_{\text{vac}}\text{-3A-In}$) with the micro grain size are even lower than the samples with the nano grains. With the optimized doping amount of In, the zT of $\text{Cu}_{\text{vac}}\text{-3A-In}$ can approach 1 at 800 K. The SPB model predicts the optimized zT for $\text{Cu}_{2-x}\text{In}_x\text{Se}$ that could reach to 1.8 at 800 K if n could be further reduced.

Chapter 2

Experimental Methods

2.1 Materials Synthesis Methods

2.1.1 Conventional Sintering Method

Pure metals with 99.99% purity were chosen as raw materials. The raw materials were weighed in the glove box and mixed manually. After obtained the mixture, the stoichiometric powder was sintered in a quartz tube at 1453 K for 2 hours. Then, the as-prepared ingot was manually ground with a mortar and pressed into discs under a force of 300 MPa in a stainless mold with a diameter of ~13 mm. For each disc, the sample weight was ~0.7 g. The pressed samples were transferred into the tube furnace for further heat treatment. For the heat treatment, the sintering temperature was 973 K with a dwelling time of 2 hours. The sintering conditions will be detailed in each subsequent chapter.

2.2 Measurement of Transport Properties

2.2.1 Seebeck Coefficient and Electrical Conductivity Measurements

The electron transport properties including both the S and the σ were measured in a helium atmosphere with a thermal system (Netzsch SBA 458 Nemesis, Germany) using the four-wire method. The testing temperature was set from room temperature to 973 K with a step of 50 K. Two pairs of thermocouples and current pins were placed under the sample for the measurements. For the σ measurement, the maximum constant current is 8 mA while the maximum heating voltage

is 8 V, producing the temperature difference of ~ 3 K. The voltage was measured by a pair of the thermocouple, spring-loaded to the surface of the sample surface. The furnace was then manually evacuated or filled with inert gas or continuously purged with inert gas. During the measurement of the S , the real-time temperature, T and thermoelectric voltage, V were recorded and plotted as a V - T plot to obtain the slope of voltage and temperature. The final S was then determined according to the following equation:

$$S = \frac{1}{2} \left(\frac{a_A + a_B}{a_B - a_A} * S_{AB} + S_A + S_B \right) \quad (2.1)$$

where a_A and a_B are the slopes of the V - T plot related to the measurement probe type: n-type for a_A and p-type for a_B . S_{AB} is the contact potential difference of thermocouple. S_A and S_B represent the thermoelectric voltages for the n-type and p-type thermocouples, respectively.

2.2.2 Thermal Conductivity Measurement

The κ_{tot} was obtained by measuring the thermal diffusivity, D , the specific heat capacity, c_p , and the geometric density, d , as a function of T , and then calculated using the following equation:

$$\kappa_{tot} = D(T)d(T)c_p(T) \quad (2.2)$$

The D was measured in an argon atmosphere by a laser flash analysis unit (Netzsch LFA 457 MicroFlash, Germany). The c_p was measured by using the sapphire method, and d is the geometric density of the bulk material measured. The measurement accuracy under the whole range was 5% according to the specifications of LFA 457.

2.2.3 Hall Coefficient Measurement

The Hall coefficient measurement was conducted using a home-made system. The Hall coefficient, R_H , was measured based on the Van der Pauw method under a DC magnetic field of 1.5-2.0 T under vacuum. The driving current and the measured voltage of the sample in the Van der Pauw method for different purposes are shown in Figure 2.1. Assuming the material is characterized by a single band, the Hall carrier concentration, $n_H = \frac{1}{R_H q_e}$, and the Hall mobility, $\mu_H = R_H \sigma$ are valid.

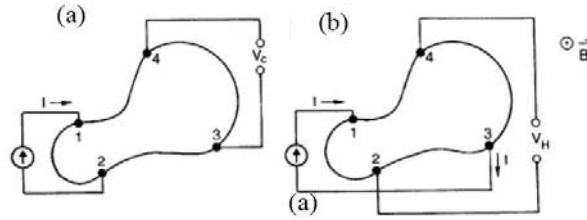


Figure 2.1 Van der Pauw approach for the measurements of (a) ρ and (b) R_H (Elton et al., 2003).

As shown in Figure 2.1, the testing sample can be with an arbitrary shape, and the probes can also be randomly attached. For case (a), a current (I_{21}) is applied from probe 2 to 1 while the voltage V_c is measured between contacts 3 and 4 ($V_{34} = V_3 - V_4$). By using Ohm's law, the resistance of the sample is written as $R_{32,41} \equiv \frac{V_{34}}{I_{21}}$ under the case (b) in Figure 2.1. Thus, without applying the magnetic field ($B_{mag} = 0$), the electrical resistivity, ρ of the sample is calculated using the following equation:

$$\rho = \frac{\pi d_{thick}}{\ln(2)} \left(\frac{R_{21,34} + R_{32,41}}{2} \right) f_{cor} \quad (2.3)$$

where d_{thick} is the sample thickness, and f_{cor} is a correction factor determined from:

$$\frac{Q-1}{Q+1} = \frac{f_{cor}}{\ln(2)} \operatorname{arccosh} \left[\frac{1}{2} \exp \left(\frac{\ln(2)}{f_{cor}} \right) \right] \quad (2.4)$$

where $Q = \frac{R_{21,34}}{R_{32,41}}$ if this ratio is larger than unity. Otherwise, $Q = \frac{R_{32,41}}{R_{21,34}}$.

It is more accurate to further average ρ by including the remaining two contact permutations, and also reversing the current polarity for all four permutations. Then,

$$\rho = \frac{\pi d_{thick}}{\ln(2)} \left[\frac{(R_{21,34} - R_{12,34} + R_{32,41} - R_{23,41}) f_A}{8} + \frac{(R_{43,12} - R_{34,12} + R_{14,23} - R_{41,23}) f_B}{8} \right] \quad (2.5)$$

where f_A, f_B are determined from Q_A and Q_B , respectively:

$$Q_A = \frac{R_{21,34} - R_{12,34}}{R_{32,41} - R_{23,41}} \quad (2.6)$$

$$Q_B = \frac{R_{43,12} - R_{34,12}}{R_{14,23} - R_{41,23}} \quad (2.7)$$

The Hall voltage V_H of the sample is determined using the situation in Figure 2.1(b), in which the current and voltage contacts are crossed. The R_H , becomes:

$$R_H = \frac{d_{thick}}{B_{mag}} \left(\frac{R_{31,42} + R_{42,13}}{2} \right) \quad (2.8)$$

In general, to minimize the error, the R_H should be obtained by averaging the values over different combinations of current and magnetic field polarities:

$$R_H = \frac{\frac{d_{thick}}{B_{mag}} [R_{31,42}(+B_{mag}) - R_{31,42}(-B_{mag}) + R_{42,13}(+B_{mag}) - R_{42,13}(-B_{mag})]}{8}$$

$$+ \frac{d_{thick}}{B_{mag}} [R_{13,42}(-B_{mag}) - R_{31,42}(-B_{mag}) + R_{24,13}(-B_{mag}) - R_{42,13}(-B_{mag})] \quad (2.9)$$

Chapter 3

Thermoelectric Charge Transport Modeling

Charge transport is not regarded as the behavior of a specific electron in the solid-state materials. Instead, the static behavior of electrons is of concern. Empirical theories of classical physics have been used to quantitatively describe the behavior or evaluate the characteristics of the electron under the electric field or heat flow. This chapter focuses on the derivation of the model related to the transport of electrons under the internal and external stimulus. Then, the physical parameters are introduced to bridge the technical parameters to the fundamental measurable physical quantities. Finally, the thermoelectric efficiency can be related to the reduced chemical potential, η , n , and T .

3.1 Boltzmann Transport Equation

The possibility of an electron appearing in the solid-state material is a function of time t , position x in the material and momentum p of the electron in the material. A function f , a distribution function, is constructed as a simple linear combination of all the contributing parts. The Boltzmann transport equation is used to depict the variation of this distribution function with respect to t , x and p :

$$df = \frac{\partial f}{\partial t} dt + \frac{\partial f}{\partial x} dx + \frac{\partial f}{\partial p} dp \quad (3.1)$$

When considering the electron collisions, p can be expressed as $\hbar k$ in which \hbar is the reduced Planck constant and k is the wave vector. Eq.(3.1) is then transformed as follows:

$$\frac{df}{dt} = \frac{\partial f}{\partial t} + \dot{x} \frac{\partial f}{\partial x} + \dot{k} \frac{\partial f}{\partial k} dk = \left(\frac{\partial f}{\partial t} \right)_{coll} \quad (3.2)$$

The dot operator stands for the derivation of the parameter. The last term in Eq.(3.2) is defined as:

$$\left(\frac{\partial f}{\partial t}\right)_{coll} = -\frac{f - f_0}{\tau} \quad (3.3)$$

where τ represents the electron relaxation time that is a conceptual parameter of the time in which an electron experiences successive collisions (to electrons, phonons or impurities). The f and f_0 are the perturbed and unperturbed distribution functions. To solve this Boltzmann transport equation, the condition is simplified by considering the conductor or semiconductor as a long rectangular electrically isotropic bar. With the Boltzmann equation, the distribution function change is considered during the relaxation time regarding to the external electric field E_{ext} . At the same time, the Fermi level E_F changes against the position and temperature difference across the sample.

The force, F , on an electron with the mass, m , the velocity, v , and the charge, q_e , under an external electric field, E_{ext} , is supposed to be:

$$F = m \frac{dv}{dt} = \hbar \frac{dk}{dt} = -q_e E_{ext} \quad (3.4)$$

With the relationship of $k = p/\hbar$, the third part of Eq.(3.2) can be transferred to

$$\hbar k \frac{\partial f}{\partial k} = q_e E_{ext} \cdot v \frac{\partial f}{\partial E} \quad (3.5)$$

Since the distribution function f is a function of $\frac{\varepsilon - E_F}{k_B T}$, Boltzmann constant, k_B , and energy variable, ε , can be defined in the Fermi-Dirac distribution:

$$f_F(\varepsilon) = \frac{1}{e^{\left(\frac{\varepsilon - E_F}{k_B T}\right)} + 1} \quad (3.6)$$

If a new parameter $\Psi = \frac{\varepsilon - E_F}{k_B T}$ is defined, then

$$\frac{\partial \Psi}{\partial T} = -\frac{1}{k_B T} \frac{\partial E_F}{\partial T} - \frac{\varepsilon - E_F}{k_B T^2} \quad (3.7)$$

and

$$v \frac{\partial f}{\partial x} = v \frac{\partial f}{\partial T} \frac{\partial T}{\partial x} = v \frac{\partial f}{\partial \Psi} \frac{\partial \Psi}{\partial T} \frac{\partial T}{\partial x} \quad (3.8)$$

Thus, the Boltzmann function can be reduced to:

$$\frac{f - f_0}{\tau} = v \frac{\partial f}{\partial E} \left(q_e E_{ext} + \frac{\partial E_F}{\partial x} + \frac{\varepsilon - E_F}{T} \frac{\partial T}{\partial x} \right) \quad (3.9)$$

The above equation can be simplified if the conductor is an open circuit with no temperature gradient and no electron flow such that $f - f_0 = 0$:

$$E_{total} = E_{ext} + \frac{1}{q_e} \frac{\partial E_F}{\partial x} \quad (3.10)$$

where E_{total} is the sum of E_{ext} and the gradient of the Fermi energy. When $E_{ext} = 0$, which is the usual case when the S is under measurement, the above equation is reduced to:

$$E_{total} = \frac{1}{q_e} \frac{\partial E_F}{\partial x} \quad (3.11)$$

Finally, assuming that the electron scattering time is too short to introduce the distribution change, the perturbed distribution in the right side of Eq.(3.9) can be replaced by an unperturbed distribution function:

$$f = \tau \cdot v \frac{\partial f_0}{\partial E} \left(\frac{\partial E_F}{\partial x} + \frac{\varepsilon - E_F}{T} \frac{\partial T}{\partial x} \right) \quad (3.12)$$

3.2 Single Parabolic Band Model

For semiconductors, the Fermi energy level is usually located in the band gap, which is much lower than the conduction band edge. The power law model assumes that the electron relaxation time has a power relationship with energy, E ,

$$\tau = \tau_{const} E^r \quad (3.13)$$

where r is the scattering parameter and τ_{const} is a constant.

To simplify the application of the SPB theory, the reduced energy, E^* , and the reduced Fermi energy, E_F^* , are used with their definitions shown below:

$$E^* = \frac{E}{k_B T} = \epsilon \quad (3.14)$$

$$E_F^* = \frac{E_F}{k_B T} = \eta \quad (3.15)$$

Thus, the power law can be modified to

$$\tau = \tau_{const} (k_B T)^r E^{*r} = \tau_0 E^{*r} \quad (3.16)$$

Assuming $\tau_0 = \tau_{const} (k_B T)^r$, the density of state function $g(E)$ is

$$g(E) = \frac{N_v}{2\pi^2} \left(\frac{2m_d^*}{\hbar^2} \right)^{\frac{3}{2}} (k_B T)^{\frac{1}{2}} E^{*\frac{1}{2}} \quad (3.17)$$

where N_v is the number of bands and m_d^* is the density-of-state effective mass.

$$m_d^* = (m_x m_y m_z)^{\frac{1}{3}} \quad (3.18)$$

where m_x, m_y, m_z are the principal effective masses in the principle-directions.

The electron concentration, n , is expressed as

$$n = \int_0^{\infty} g(E)f(E)dE \quad (3.19)$$

where $f(E)$ is the occupation probability. The Fermi-Dirac distribution $f_F(E)$ takes place when n is:

$$n = \int_0^{\infty} g(E)f_F(E)dE \quad (3.20)$$

Then, n is transformed to:

$$n = \frac{N_v}{2\pi^2} \left(\frac{2m_d^*k_B T}{\hbar^2} \right)^{\frac{3}{2}} \int_0^{\infty} \frac{(E^*)^{\frac{1}{2}}}{e^{(E^* - E_F^*)} + 1} dE^* \quad (3.21)$$

Here the Fermi integral, F_s , is defined as an integral as:

$$F_s = \int_0^{\infty} \frac{\epsilon^s}{e^{(\epsilon - \eta)} + 1} d\epsilon \quad (3.22)$$

Thus, n is simplified as

$$n = \frac{N_v}{2\pi^2} \left(\frac{2m_d^*k_B T}{\hbar^2} \right)^{\frac{3}{2}} F_{\frac{1}{2}} \quad (3.23)$$

The connection between n and current density, j , can be seen below:

$$j = \mp n q_e v_x \quad (3.24)$$

where j is the current density in the x-direction and v_x is the velocity in the x-direction;

$$j = \mp \int_0^{\infty} q_e v_x g(E)f(E)dE \quad (3.25)$$

$$j = \mp \frac{2(2m)^{\frac{1}{2}}q_e}{3\pi^2\hbar^3} \int_0^\infty E^{\frac{3}{2}}\tau \frac{\partial f_0}{\partial E} \left(\frac{\partial E_F}{\partial x} + \frac{E - E_F}{T} \frac{\partial T}{\partial x} \right) dE \quad (3.26)$$

With the definition of $\sigma = j / E = \frac{j}{\frac{1}{q_e} \frac{\partial E_F}{\partial x}}$, σ is expressed as below (Rowe, 2012; Lee, 2017):

$$\sigma = \int_0^\infty \sigma(E) \frac{\partial f_0}{\partial E} dE \quad (3.27)$$

where

$$\sigma(E) = \frac{2(2m)^{\frac{1}{2}}}{3\pi^2\hbar^3} q_e^2 E^{\frac{3}{2}} \tau \quad (3.28)$$

Thus,

$$\sigma = \frac{N_v q_e^2 \tau_0}{3\pi^2 m_c^*} \left(\frac{2m_d^* k_B T}{\hbar^2} \right)^{\frac{3}{2}} \left(r + \frac{3}{2} \right) F_{r+\frac{1}{2}} \quad (3.29)$$

According to the definition of $\sigma = n q_e \mu$, μ is electron mobility. Eq.(3.29) is transformed with the property that:

$$\int_0^\infty \phi(E) \frac{\partial f_0(E)}{\partial E} dE = - \int_0^\infty f_0(E) \frac{\partial \phi(E)}{\partial E} dE, \text{ where } \phi(0) = 0 \quad (3.30)$$

σ can be derived as,

$$\sigma = \left[\frac{N_v}{2\pi^2} \left(\frac{2m_d^* k_B T}{\hbar^2} \right)^{\frac{3}{2}} F_{\frac{1}{2}} \right] q_e \left[\frac{q_e \tau_0}{m_c^*} \frac{2}{3} \left(r + \frac{3}{2} \right) \frac{F_{r+\frac{1}{2}}}{F_{\frac{1}{2}}} \right] \quad (3.31)$$

The definition of electron mobility, μ is thus

$$\mu = \frac{q_e \langle \tau \rangle}{m_c^*} \quad (3.32)$$

where m_c^* is the conductive effective mass.

Actually, μ and n cannot be directly accessible by Hall measurement. With the relationship of $R_H = \frac{1}{n_H q_e}$, n_H can be obtained from the measured Hall coefficient R_H . And r_H is also a function of the Fermi integral, F_S .

$$r_H = \frac{3}{2} F_1 \frac{F_{-\frac{1}{2}}}{2F_0^2} \quad (3.33)$$

$$n_H = N_v 4\pi \left(\frac{2m_d^* k_B T}{\hbar^2} \right)^{\frac{3}{2}} \frac{F_1}{r_H} \quad (3.34)$$

The measured μ_H is the function of F_S with a constant μ_0 , called the mobility factor. This can only be valid when a single parabolic band semiconductor is considered:

$$\mu_H = \mu_0 \frac{\left(\frac{1}{2} + 2 \left(r + \frac{1}{2} \right) \right) F_{2 \left(r + \frac{1}{2} \right) - \frac{1}{2}}}{\left(1 + \left(r + \frac{1}{2} \right) \right) F_{r + \frac{1}{2}}} \quad (3.35)$$

This μ_0 has its physical significance, depending on the electron scattering mechanism. If the acoustic phonon scattering dominates, μ_0 can be regarded as the mobility of a single charge carrier in a nondegenerate band (lightly doped). This also requires the value of r to be $-1/2$.

The theoretical tendency of μ_H against temperature in a log-log coordinates shows a line with a slope to be -1.5 (Figure 3.1). The curve can be moved vertically in the μ_H vs T log-log figure to verify the real data. There also might be the case that the slope is not exactly equal to -1.5 , which is also acceptable if the value ranges from -1 to -1.5 . Otherwise, other electron scattering mechanism will be considered, if the SPB model is used.

$$\mu_H = \mu_0 \frac{F_{-1/2}}{2F_0} \quad (3.36)$$

Here $\mu_0 = \mu_{0,l}$ is re-defined:

$$\mu_{0,l} = \frac{q_e \pi \hbar^4}{\sqrt{2} (k_B T)^{\frac{3}{2}} E_{def}^2 (m_d^*)^{\frac{5}{2}}} C_{11} \quad (3.37)$$

where C_{11} is the elastic constant for longitudinal vibrations, E_{def} is the deformation potential, and m_d^* is the density of states effective mass. The subscript of l in $\mu_{0,l}$ denotes that the quantity solely refers to the case of scattering by the acoustical vibrations of the lattice atoms.

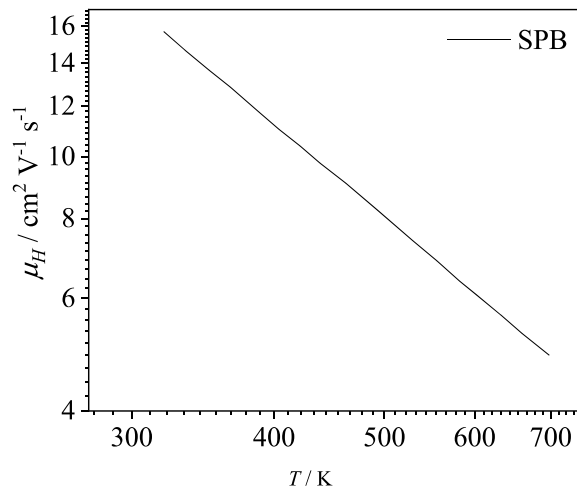


Figure 3.1 The μ_H curve as a function of temperature plotted in a log-log format by using the SPB model, assuming the interaction of phonons and electrons are mainly due to the acoustic phonon scattering at medium and high temperatures.

With Eqs.(3.24), (3.25), (3.27) and (3.28), a typical relationship of μ_H to the n at specific temperatures can be obtained as shown in Figure 3.2.

As shown in Figure 3.2, the data of the SPB model shows the general relationship between μ_H and n_H . Typically, when n_H decreases, μ_H increases. Moreover, the temperature could also enhance the scattering, resulting in the degradation of μ_H . The curves shown in Figure 3.2 can also be used to determine m_d^* when the data of the doped parent material is obtained in the specific temperature. The reliable value of m_d^* is chosen when the theoretical curve fits the experimental data well.

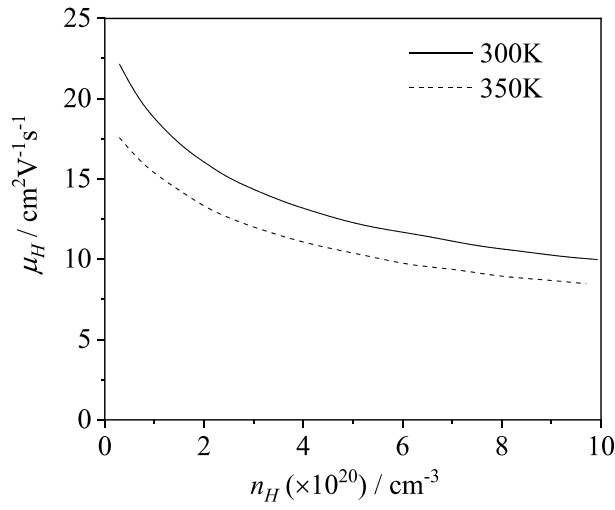


Figure 3.2 Room-temperature μ_H curve as a function of n_H . The parameters at 300 K and 350 K are represented by a solid line and a dashed line, respectively. $m_d^*=1.86m_e$, $C_{11} = 116.3 - 0.0208T$ (300 K < T < 900 K), $E_{def} = 8.3$ eV.

S is also a function of the reduced Fermi level. Once S is obtained from the measurement, η is derived. It should be noted that S is only dependent on η in the SPB model.

$$S = -\left(\frac{k_B}{q_e}\right) \left[\frac{\left(r + \frac{5}{2}\right) F_{r+\frac{3}{2}}}{\left(r + \frac{3}{2}\right) F_{r+\frac{1}{2}}} - E_F^* \right] \quad (3.38)$$

m_d^* can be derived with the measured S and the n_H at the specific temperature. Using Eqs.(3.25) and (3.30). a plot of S as a function of n_H , the Pisarenko plot, can be obtained as shown in Figure 3.3.

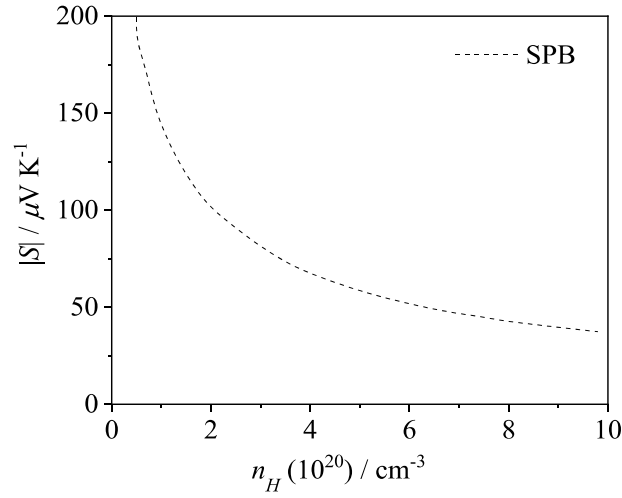


Figure 3.3 The absolute value of the room-temperature S calculated by the SPB model.

The Lorenz number L_0 can be plotted by using the equation below:

$$L_0 = \left(\frac{k_B}{q_e}\right)^2 \left\{ \frac{\left(r + \frac{7}{2}\right) F_{r+\frac{5}{2}}}{\left(r + \frac{3}{2}\right) F_{r+\frac{1}{2}}} - \left[\frac{\left(r + \frac{5}{2}\right) F_{r+\frac{3}{2}}}{\left(r + \frac{3}{2}\right) F_{r+\frac{1}{2}}} \right]^2 \right\} \quad (3.39)$$

With Eq.(3.39), the electronic contribution κ_e and κ_{tot} can be derived, and the lattice contribution κ_l can be estimated according to the below equations:

$$\kappa_e = L_0 \sigma T \quad (3.40)$$

$$\kappa_l = \kappa_{tot} - \kappa_e = \kappa_{tot} - L_0\sigma T \quad (3.41)$$

If the longitudinal velocity, v_l and transverse velocity, v_t are obtained, then according to Cahill et al. (M. C. Wingert et al., 2016), the limitation of lattice thermal conductivity, κ_{lmin} for amorphous materials can be derived:

$$\kappa_{lmin} = \frac{1}{2} \left(\frac{\pi}{6}\right)^{\frac{1}{3}} k_B V_{atom}^{-\frac{2}{3}} (2v_t + v_l) \quad (3.42)$$

where V_{atom} is the atomic volume.

The thermoelectric efficiency, zT can be calculated at a specific temperature:

$$zT = \frac{S^2\sigma T}{k_e + k_l} \quad (3.43)$$

And when

$$zT = \frac{S^2\sigma T}{L_0\sigma T + k_l} = \frac{S^2}{L_0 + (\psi\beta)^{-1}} \quad (3.44)$$

where function ψ and β are:

$$\psi = \frac{8\pi q_e}{3} \left(\frac{2m_e k_B}{h^2}\right)^{\frac{3}{2}} F_0 \quad (3.45)$$

$$\beta = \mu_0 \left(\frac{m^*}{m_e}\right)^{\frac{3}{2}} \frac{T^{\frac{5}{2}}}{k_l} \quad (3.46)$$

3.3 Quality Factor

For superionic materials, the Hall mobility is too small to be measured with good reliability. One of the ways to tackle this is to avoid the calculation of the η . From Equation 3.44,

$$zT = \frac{S^2 \sigma T}{L_0 \sigma T + k_l} = \frac{S^2}{L_0 + \frac{k_l}{\sigma T}} \quad (3.47)$$

With $\sigma = \sigma_{E_0} \ln(1 + e^\eta)$,

$$zT = \frac{S^2 \sigma T}{L_0 \sigma T + k_l} = \frac{S^2}{L_0 + \frac{k_l}{T \sigma_{E_0} \ln(1 + e^\eta)}} = \frac{S^2}{L_0 + \frac{\left(\frac{k_B}{q_e}\right)^2}{B \ln(1 + e^\eta)}} \quad (3.48)$$

where quality factor, B is equal to

$$B = \left(\frac{k_B}{q_e}\right)^2 \frac{\sigma_{E_0}}{\kappa_l} T \quad (3.49)$$

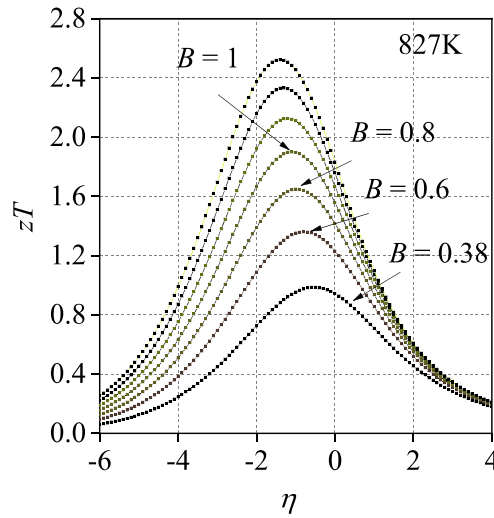


Figure 3.4 zT vs η with different B of the thermoelectric material.

Compared with β , B is the dimensionless quality factor that is convenient to be used to characterize the thermoelectric material.

Figure 3.4 shows the plot of zT vs η with different B of the thermoelectric material. It can be seen that the SPB model gives a clear presentation of the relationship between zT and η . Higher B would enhance the zT value and shift the optimized η to the lower value, which implies that lower n and higher S are more favorable.

Chapter 4

Thermoelectric Performance and Modeling for Cu_{2-x}Se Fabricated Using the Conventional Sintering Method

In this chapter, the thermoelectric properties of Cu_{2-x}Se fabricated using the conventional sintering method will be explored systematically. Moreover, the repeatability of the materials during the thermal cycles will also be studied. In detail, the repeatability of Cu_{2-x}Se is attempted to investigate in terms of raw material, testing condition, and Cu vacancy. Moreover, the SPB model described in Chapter 3 is utilized to describe the electron transport characteristics.

4.1 Materials Preparation

Cu_{2-x}Se samples were synthesized by the conventional solid-state sintering method. Cu was reduced at 773 K for 2 hours with a flow of 5% H_2 -Ar, and Se (99.99%) were used as the raw materials. The weight of the raw materials was calculated according to the chemical formula. The mixture was sealed in a quartz crucible, melted at 1453 K for 2 hours, and annealed at 973 K for 10 hours. The heat treatment of Cu_{2-x}Se can be seen in Figure 4.1. The Cu_{2-x}Se samples are denoted as $\text{Cu}_{\text{vac}}-(x \times 100)$, for example, the $\text{Cu}_{1.97}\text{Se}$ and $\text{Cu}_{1.94}\text{Se}$ samples are denoted as $\text{Cu}_{\text{vac}}-3$ and $\text{Cu}_{\text{vac}}-6$, respectively.

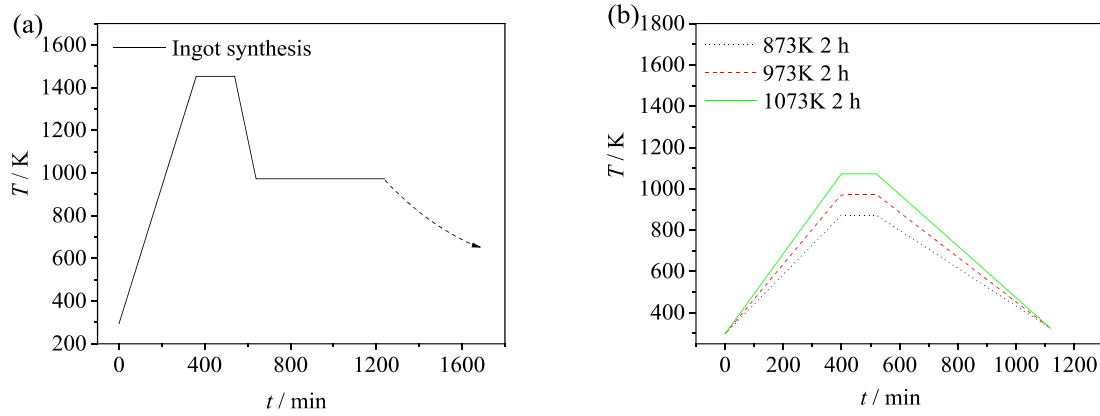


Figure 4.1 Heating treatment process for Cu_{2-x}Se . (a) Heat treatment for ingot synthesis with cooling inside the furnace to room temperature, (b) heat treatment for bulk samples synthesis at different sintering temperatures for 2 hours with the controlled cooling rate.

Then, the as-prepared ingot was ground into fine powder using an agate mortar, weighed, and pressed into discs under a pressure of 300 MPa. Finally, the discs with a diameter of ~ 13 mm were sintered again at 973 K for 2 hours, respectively, and then slowly cooled down to room temperature. The detailed heat treatment is shown in Figure 4.1(b).

4.2 Results and Discussion

4.2.1 Microstructural Properties

To explore the phase structure of Cu_{2-x}Se , the PXR measurement was performed and results are shown in Figures 4.2 (a) – (c) together with standard PDF cards diffraction peaks. As can be seen, all the samples show Cu_{2-x}Se or Cu_2Se phase without any other impurity. Moreover, phase structure becomes more complicated with a large amount of Cu vacancy. For example, the $\text{Cu}_{\text{vac}}-6$ shows a mixture of orthorhombic Cu_2Se_x (PDF # 47-1448) phase and cubic Cu_2Se phase (PDF

#06-0680), while, monoclinic Cu_2Se (PDF # 27-1131) phase is preferable in the $\text{Cu}_{\text{vac-3}}$. When the Cu vacancy density is reduced to 0.01, the low-temperature phase structure turns to be an orthorhombic Cu_{2-x}Se phase.

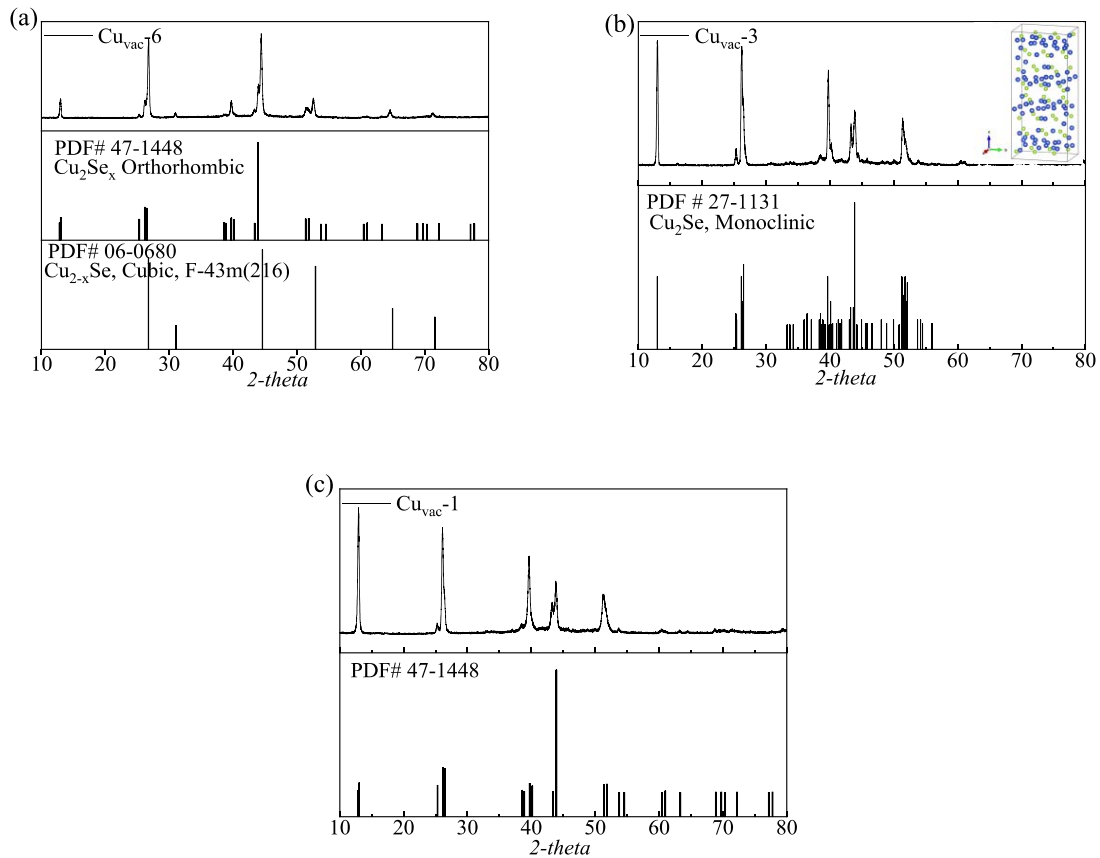


Figure 4.2 Powder X-ray diffraction (PXRD) patterns measured at room temperature for (a) $\text{Cu}_{1.94}\text{Se}$ ($\text{Cu}_{\text{vac-6}}$) sintered at 973 K. (Black column bars show the standard PDF card #47-1448 diffraction peak sites for the orthorhombic Cu_2Se_x phase and PDF card #06-0680 diffraction peak sites for the high-temperature cubic phase Cu_{2-x}Se), (b) $\text{Cu}_{1.97}\text{Se}$ ($\text{Cu}_{\text{vac-3}}$) sintered at 973 K. (Black column bars show the standard PDF card #27-1131 diffraction peak sites for the low-temperature monoclinic Cu_2Se phase), (c) $\text{Cu}_{1.99}\text{Se}$ ($\text{Cu}_{\text{vac-1}}$) sintered at 973K. (Black column bars show the standard PDF card #47-1448 diffraction peak sites for the low-temperature Monoclinic Cu_2Se phase)

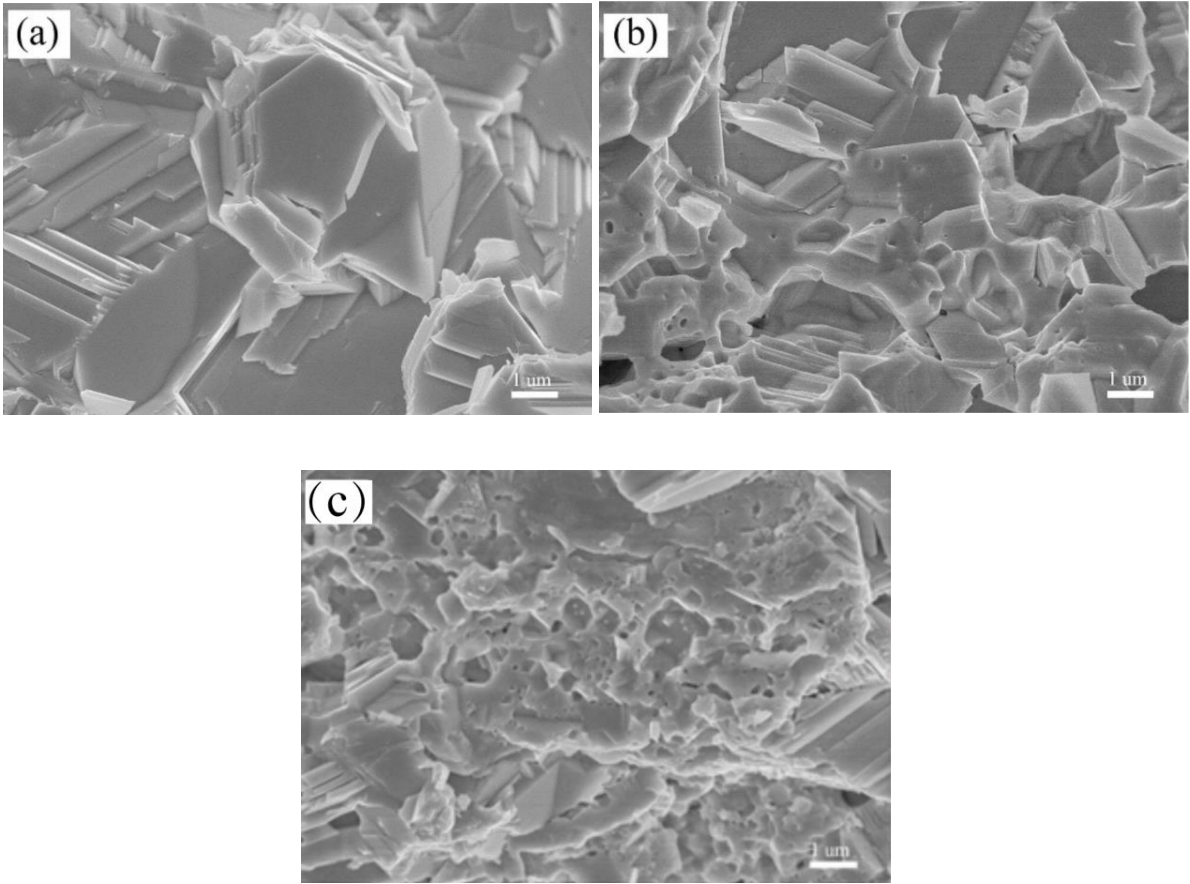


Fig. 4.3 SEM images for the cross-sections of the as-sintered (a) $\text{Cu}_{\text{vac}-6}$, (b) $\text{Cu}_{\text{vac}-3}$, and (c) $\text{Cu}_{\text{vac}-1}$.

4.2.2 Thermoelectric Performance

Figure 4.4 shows the thermoelectric performance of the Cu_{2-x}Se samples during the heating and cooling cycles. It is obviously seen that a phase transition happens for all the samples between 350 K to 400 K where a turning point is shown in the σ curves (Figure 4.4 (a)). The data obtained from different samples display different levels of data repeatability from the heating to cooling curves. For $\text{Cu}_{\text{vac}-1}$, large deviations can be observed even though the annealing time has been elongated to obtain more homogeneous microstructure. However, the deviations for other samples with large Cu vacancy become smaller and even diminish for the $\text{Cu}_{\text{vac}-6}$, showing the excellent repeatability.

The same phenomenon also happens for the results of S , which is shown in Figure 4.3 (b). For power factor, PF , both the samples with Cu vacancy also shows the excellent repeatability as shown in Figure 4.4 (c), which is more favorable for the superionic material to be used in the practical application. However, it should be noted that the PF does not coincide well below 400 K, which is attributed to be the first order phase transition (S. D. Kang et al., 2017). This noncoincidence might also comes from the complexity of the low-temperature structure of Cu_{2-x}Se dimensions due to the phase transition.

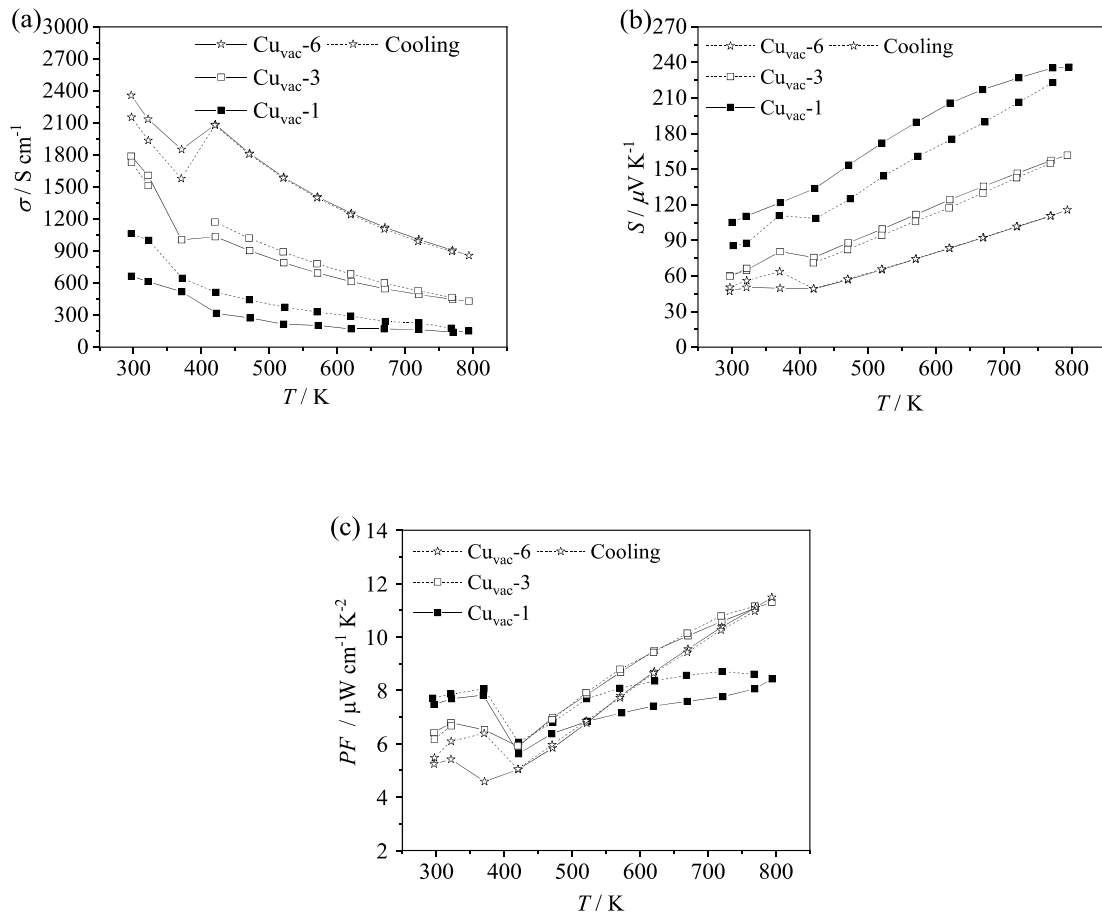


Figure 4.4 Temperature dependence of (a) σ , (b) S and (c) PF for Cu_{2-x}Se sintered at 973 K for 2 hours.

The D of Cu_{2-x}Se samples was shown as a function of temperature in Figure 4.5. It is clear that the samples with higher Cu vacancy show higher D across the whole temperature range. Since the samples with a large amount of Cu vacancy usually show large σ , thus electronic thermal conductivity, κ_e contributes more to the κ_{tot} . With the measured D , the κ_{tot} data was calculated based on the definition in which the specific heat capacity c_p is evaluated by using the data from Kang's work for reference (S. D. Kang et al., 2018).

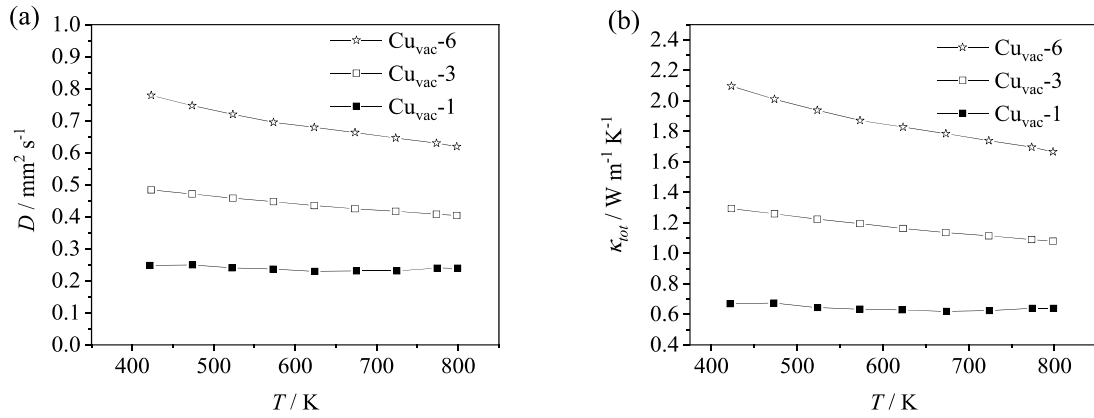


Figure 4.5 Temperature dependence of (a) D , and (b) κ_{tot} for Cu_{2-x}Se .

To analyze the electronic contribution to the κ_{tot} of the samples, the L_0 should be calculated. By using the SPB model in Chapter 3, the η can be obtained from S as a function of temperature. As stated in Chapter 3, when the SPB model is applied, the L_0 can be derived, which is also a monotone function of the η . In Figure 4.6 (a), the L_0 decreases against temperature due to the increasing η which is represented by the tendency of S .

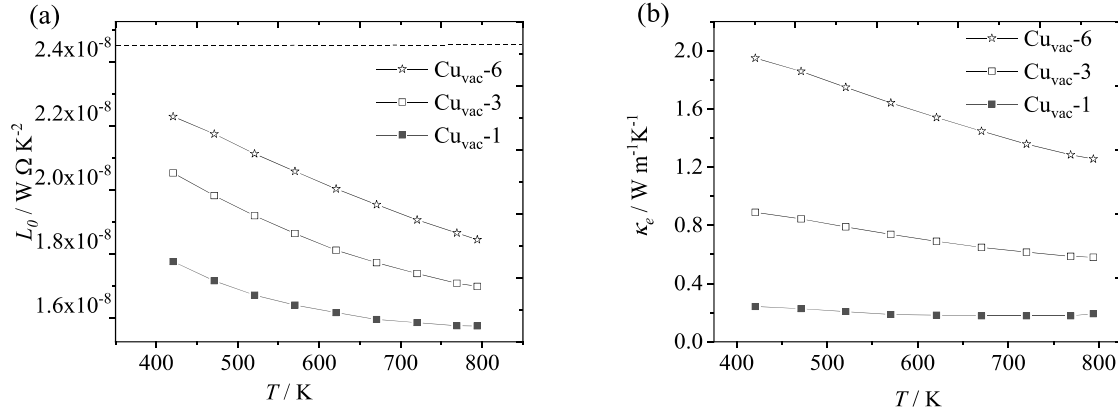


Figure 4.6 Temperature dependence of (a) L_0 of $Cu_{2-x}Se$ derived and the metallic limit represented by the dashed line, and (b) κ_e derived by using the equation $\kappa_e = L_0 \sigma T$.

The metallic limit of L_0 derived via quantum mechanical treatment is also represented by the dashed line as shown in the same figure. The metallic limit overestimates the κ_e but underestimates the κ_l .

In general, when the temperature increases, the κ_e decreases due to the enhanced phonon-electron interaction. For Cu_{vac-1} , at high temperatures (i.e., >700 K), the slight increment of κ_e indicates the physical change or phase instability of the sample, which is also demonstrated by the non-repeatable data of the σ curve as shown in Figure 4.4. A similar peak of S for Cu_2Se is observed, which might also correlate to the bipolar effect (S. D. Kang et al., 2018).

Assuming the acoustic phonon scattering dominates at the high-temperature range (>400 K), the weighted mobility, U , is evaluated to characterize the electron transport of materials (S. D. Kang et al., 2018). All the σ and S data for the high-temperature phase in Figure 4.4 were selected to evaluate the U of the materials. As shown in Figure 4.7, the U of all materials except Cu_{vac-1} is linearly proportional to the temperature. For the Cu_{vac-1} , the slight deviation of the high-

temperature data implies that the electron transport behavior is not related to the bipolar effect because the bipolar effect would dampen the U generally. To avoid other factors affecting the analysis, the instrument measurement design is claimed to eliminate the cold-finger effect that would cause an abnormal increase in weighted mobility at high temperatures. The deformation potential, E_{def} , of the Cu_{2-x}Se samples is quantitatively compared with the slope in Figure 4.7 under the assumption of having the same m_e . It is shown that the curve for Cu_{vac-6} exhibits the largest slope, which indicates that the edge of the valance band structure tends to be easily changed or correlated for the samples with more Cu vacancy. The similar behavior can be clearly seen in Figure 4.8, in which the transport coefficient σ_E is plotted as a function of temperature (S. D. Kang et al., 2018). All the curves show a linear relationship against $T^{-0.2}$, where the exponent is a fitting parameter. Typically, for a conductive polymer, a constant of -0.5 is usually used. Here, for Cu_2Se and its nonstoichiometric material with Cu vacancy, σ_E is modeled for the first time. Moreover, a slight deviation exists for Cu_{vac-1} at a high temperature range, which indicates that some physical change occurred.

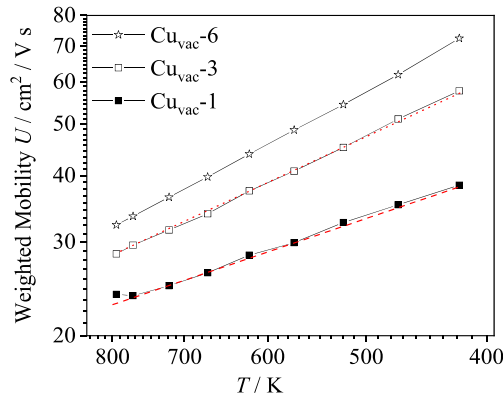


Figure 4.7 Temperature dependence of U for Cu_{2-x}Se evaluated by the S and σ measured at one single temperature.

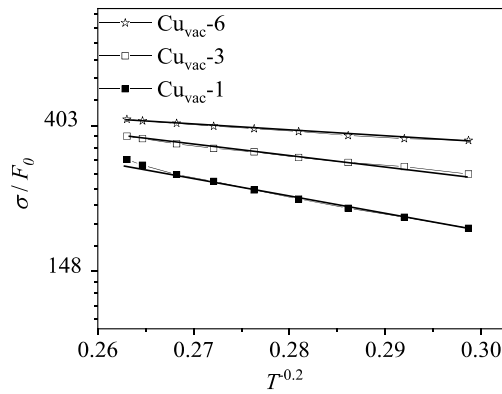


Figure 4.8 Temperature dependence of σ_E of Cu_{2-x}Se .

The carrier concentration of all samples has been measured at room temperature, and the results are presented as a function of Cu vacancy in Figure 4.9. For $\text{Cu}_{\text{vac}}-6$, the big deviation of the data might result from the mixed cubic structure. According to Figure 4.9, more Cu vacancy could increase the carrier concentration, n_q , for $\text{Cu}_{\text{vac}}-1$, $\text{Cu}_{\text{vac}}-2$ and $\text{Cu}_{\text{vac}}-3$. $\text{Cu}_{\text{vac}}-6$ shows the abnormal trend of carrier concentration due to the mixed low-temperature phase (PDF #06-0608) as shown in Figure 4.2. For the mobility data, the opposite trend to the Cu vacancy level is observed, which can be explained as the enhanced electron scattering by Cu vacancy defects.

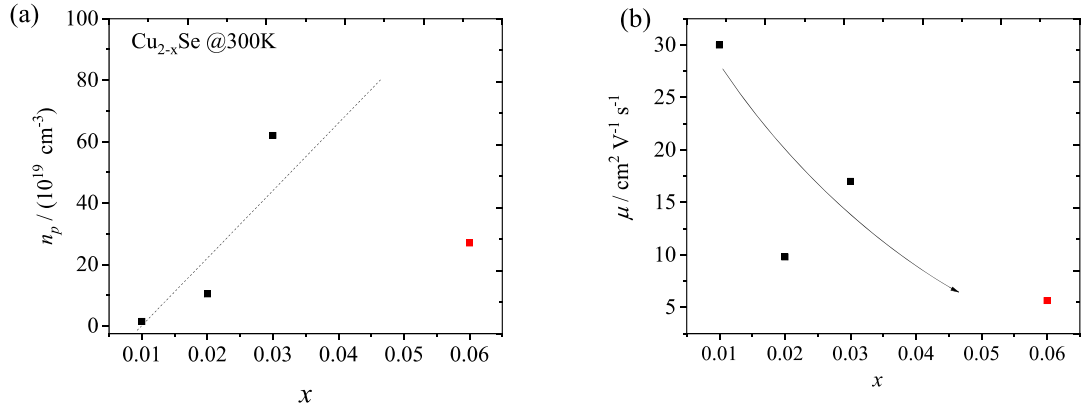


Figure 4.9. Hall carrier concentration, n_p and mobility, μ as a function of Cu vacancy content x at room temperature.

As shown in Figure 4.10(a), the measured zT and S of $\text{Cu}_{\text{vac-3}}$ are 0.831 and $161.80 \mu\text{V K}^{-1}$, respectively, which make good agreement with the calculated data from the SPB model (0.827 and $160.38 \mu\text{V K}^{-1}$ in Figure 4.10(b)). The black dash curve in Figure 4.10(b) is derived from using the S , σ , κ_{tot} , and κ_l of $\text{Cu}_{\text{vac-3}}$.

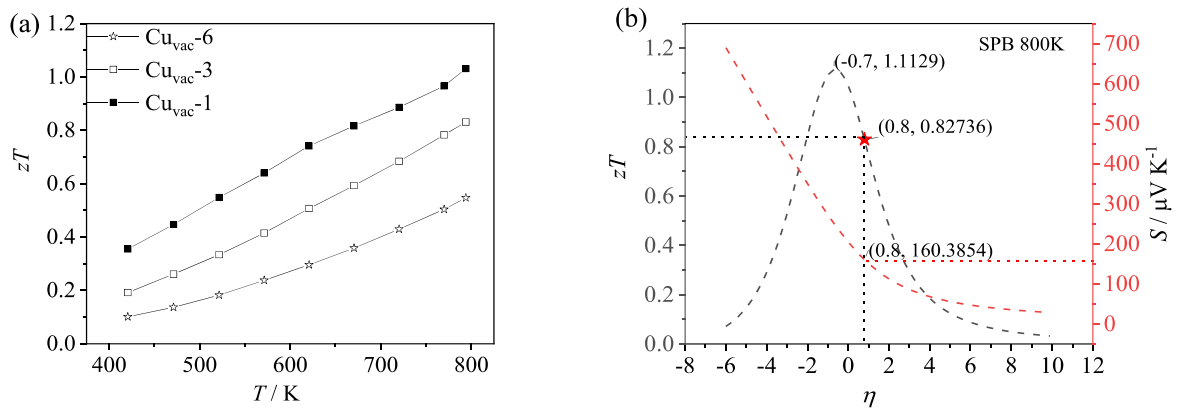


Figure 4.10 (a) Temperature dependence of zT for Cu_{2-x}Se with different Cu vacancies (dashed line represents the theoretical curve of Cu_2Se), and (b) SPB model results at 800 K (black dash line for zT and red dashed line for S) with the measured zT of $\text{Cu}_{\text{vac}-3}$ (represented by a star symbol).

The B is calculated to be 0.45 at 800 K. Although the modeling results show that the zT value could reach 1.11 at 800 K if the B is optimized, the present zT value of 0.83 is already very close to that obtained from the SPS samples (~ 0.85) (K. Biswas et al., 2012). The results prove that the Cu_2Se -based thermoelectric material with relatively good thermoelectric performance can also be fabricated using the cost-effective conventional sintering method when compared with SPS and HPS techniques.

4.3 Conclusion

Cu_{2-x}Se with Cu vacancy has been investigated concerning the data repeatability. The precise control of the raw materials, especially for Cu, could give significant data repeatability improvement. Moreover, the material with higher Cu vacancy can be more thermally stable when compared with $\text{Cu}_{\text{vac}-1}$. The zT value of $\text{Cu}_{\text{vac}-3}$ could reach 0.83 at 800 K with excellent repeatability. Moreover, from the SPB model calculation, the zT value could reach 1.11 if the B is further enhanced.

Chapter 5

Cycling Performance Study of $\text{Cu}_{1.97}\text{Se}$ Superionic Thermoelectric Materials

In this Chapter, based on the study in the previous Chapter, lead-free non-stoichiometric copper selenide, $\text{Cu}_{\text{vac}}\text{-3}$ fabricated using the conventional sintering method is selected for in-depth investigation. From the previous Chapter, the repeatability of σ , S , PF is highly related to the Cu vacancy. However, the source of repeatability is still unclear with regards to the fabrication condition. To explore the factors which affect the data repeatability besides the Cu vacancy, samples with different levels of Se evaporation were prepared using the conventional sintering method. The microstructural properties and thermoelectric performance of $\text{Cu}_{\text{vac}}\text{-3}$ are presented and discussed.

5.1 Materials Preparation

$\text{Cu}_{\text{vac}}\text{-3}$ samples were synthesized by the conventional solid-state sintering technique. The starting materials, Cu (99.9%) and Se (99.99%), were used and calculated according to the chemical formula. Then, the mixture was sealed in a quartz crucible and melted at 1453 K for 2 hours and annealed at 973 K for 10 hours. The as-prepared ingot was ground into fine powder using an agate mortar, weighed, and pressed into discs under a pressure of 300 MPa. Finally, the discs with a diameter of ~ 13 mm and a thickness of ~ 0.7 mm were sintered again at 873 K, 973 K, and 1073 K for 2 hours, respectively, and then slowly cooled down to room temperature within the tube furnace.

5.2 Results and Discussion

5.2.1 Microstructural Properties

To explore the possibility of obtaining samples with different Cu vacancy densities via changing the amount of Se evaporation during the sintering process, TGA was performed on the $\text{Cu}_{\text{vac}}\text{-3}$ powder and the result is shown in Figure 5.1. TGA measurement can also be used to evaluate the thermal stability of thermoelectric materials (U. Aydemir et al., 2016). As shown in Figure 5.1(a), the large weight loss occurred at ~ 800 K during the heating process at 1 atm with N_2 gas protection, which is close to Liu's work (H. Liu et al., 2012). Thus, in order to obtain samples with various rates of Se evaporation, the sintering temperatures were selected to be 873 K, 973 K, and 1073 K, while keeping the dwelling time constant.

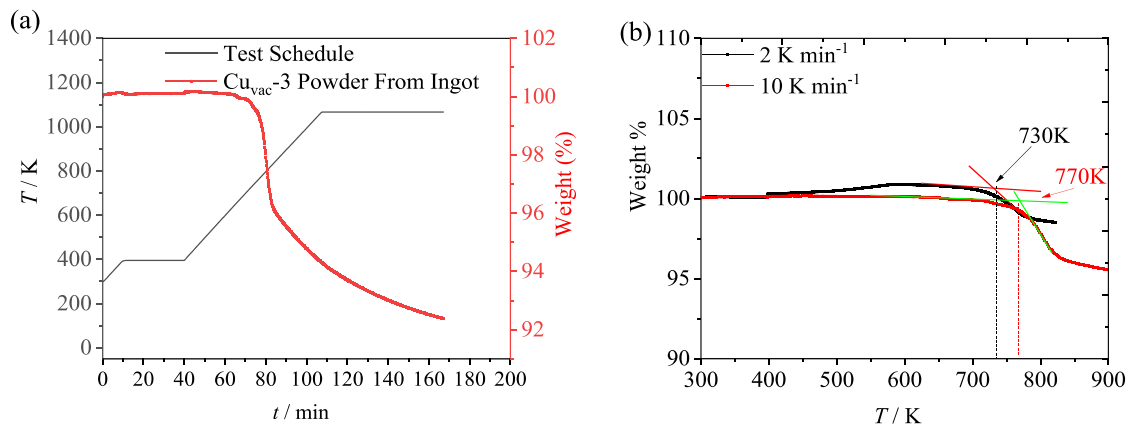


Figure 5.1 TGA curves for (a) the $\text{Cu}_{\text{vac}}\text{-3}$ powder obtained from the melt ingot, and (b) the $\text{Cu}_{\text{vac}}\text{-3}$ powder under different heating rates.

The TGA curve against the temperature with different heating rates is shown in Figure 5.1(b), in which the temperatures of Se evaporation from the Cu-Se system were 730 K for 2 K min⁻¹ and 770 K for 10 K min⁻¹, respectively. It was reported that the existence of Cu vacancies may be capable of avoiding the instability arisen from interactions between Cu^+ ions in $\alpha\text{-Cu}_2\text{Se}$ (J. Y. Tak

et al., 2018). The vacancy formation energy, ΔE , for generating one Cu vacancy in Cu_2Se is usually calculated by substituting the cohesive energy of metallic Cu from the system (K. P. Zhao et al., 2017). According to Zhao's calculation, the vacancy formation energy value is 0.15 eV, which is much larger than the thermal energy $k_B T$ of the system at 730 K ($= 0.0629$ eV). This indicates that the weight loss of $\text{Cu}_{\text{vac}}-3$ in Figure 5.1 is probably due to the evaporation of Se instead of the formation of Cu vacancy. To explore the influence of the loss of Se on the microstructure of samples, PXRD measurements were performed at room temperature (Figure 5.2).

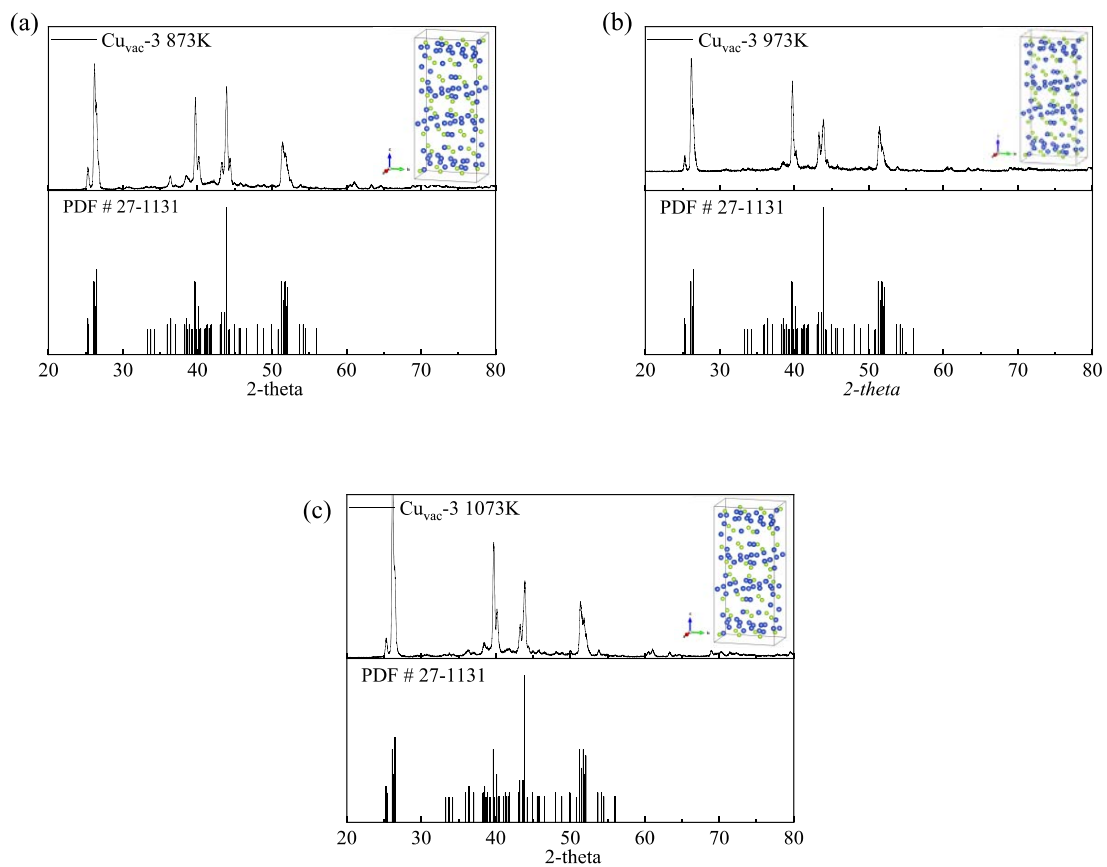


Figure 5.2 PXRD patterns for $\text{Cu}_{\text{vac}}-3$ sintered at 873 K, 973 K, and 1073 K for 2 hours. (Black column bars show the monoclinic Cu_2Se phase (standard PDF card #27-1131)).

Figure 5.2 shows the PXRD patterns for Cu_{vac}-3 sintered at 873 K, 973 K, and 1173 K for 2 hours, respectively. All the patterns exhibited identical diffraction peaks related to PDF card #27-1131, indicating that the conventional sintering technique does not produce impurities. This is consistent with Zhao's work (L. L. Zhao et al., 2015) that adopted the melting and quenching methods for samples fabrication. Besides, all the samples are shown to exhibit the low-temperature monoclinic microstructure without the involvement of other phases, which was reported in the samples fabricated using the melting and hot press method (PDF card #47-1448) (H. Liu et al., 2012) and the solvothermal technique (PDF card #06-0680) (L. Yang et al., 2016), respectively.

To analyze the influence of sintering temperature on the phase structure of as-prepared Cu_{vac}-3, Rietveld refinements were performed to evaluate the relationship between the rate of Se evaporation and lattice distortion. The corresponding results are shown in Figure 5.3 and Table 5.1, revealing that the samples sintered at higher temperatures (with higher rates of Se evaporation) have larger unit cell volume from 2410.767 Å³ to 2428.988 Å³. The values are close to those reported in Gulay's study (L. Gulay et al., 2011), in which the cell volume of stoichiometric Cu₂Se was 2414.0 Å³. When the samples were sintered at higher temperature, the rate of Se evaporation increased, resulting in the increasing Cu/Se ratio and decreasing Cu vacancy density. As Cu vacancy defects are usually associated with the distortion of the unit cell, low lattice distortion (large cell volume) can be retained for the samples sintered at high temperatures (973 K and 1073 K).

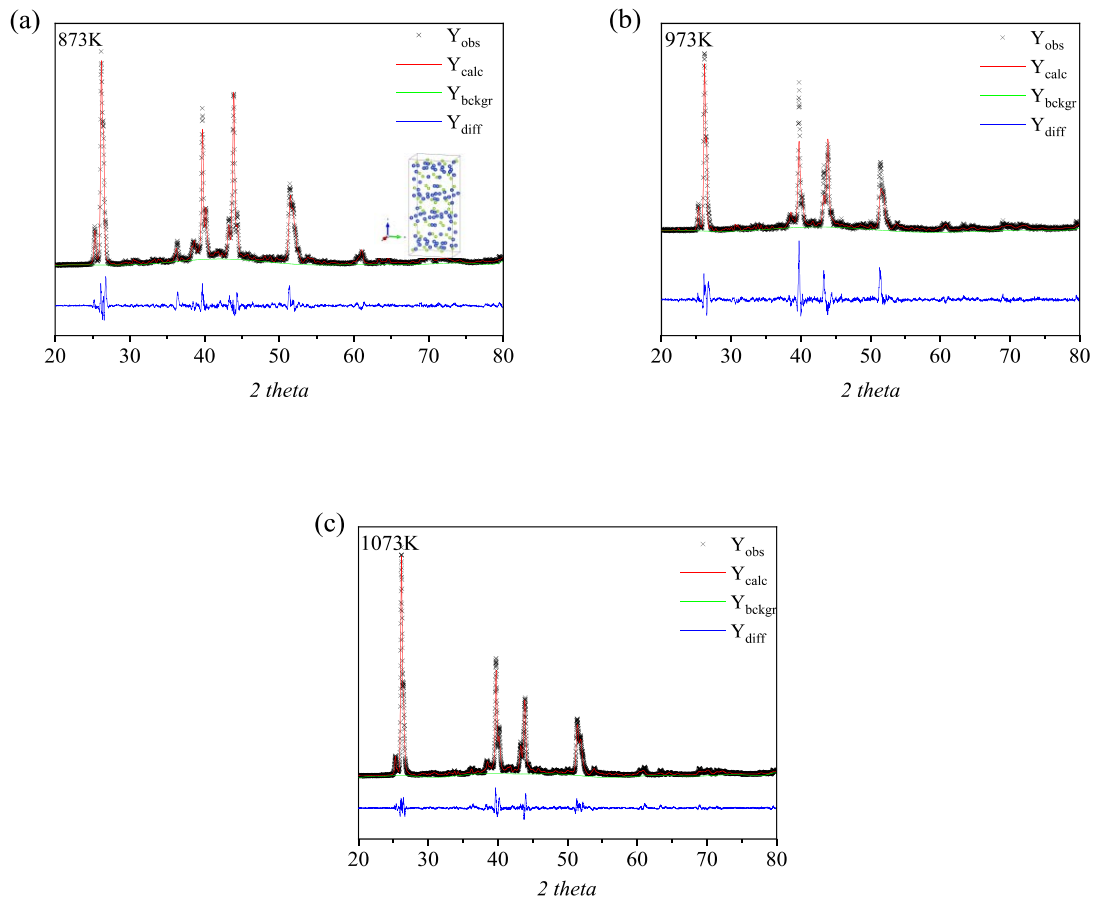


Figure 5.3 Rietveld refinements of XRD profiles of $\text{Cu}_{\text{vac-3}}$ sintered at different temperatures: (a) 873 K, (b) 973 K and (c) 1073 K.

Table 5.1 Rietveld analysis of the XRD results for $\text{Cu}_{\text{vac-3}}$.

Samples	Lattice parameters					R-factors		
	a (Å)	b (Å)	c (Å)	β	Vol (Å ³)	χ^2	R_p (%)	R_{wp} (%)
$\text{Cu}_{\text{vac-3-873K}}$	7.142	12.380	27.338	94.189	2410.767	4.413	11.53	16.14
$\text{Cu}_{\text{vac-3-973K}}$	7.171	12.379	27.410	94.453	2426.165	3.843	20.20	26.40
$\text{Cu}_{\text{vac-3-1073K}}$	7.169	12.400	27.401	94.370	2428.988	3.877	10.67	14.32

Figure 5.4 shows the typical SEM micrographs of the $\text{Cu}_{\text{vac-3}}$ sintered at different sintering temperatures. All the samples show micron grain size ranging from 1 μm to 10 μm with similar morphological and structural characteristics. With increasing the sintering temperature, the portion of small grains was shown to slightly reduce. The crystallization was well developed that is illustrated by the trans-crystalline fracture. For the morphology of samples sintered at higher temperatures, the overall grain size is enlarged but pores can still be seen that should be attributed to the evaporation of Se during the high-temperature sintering process.

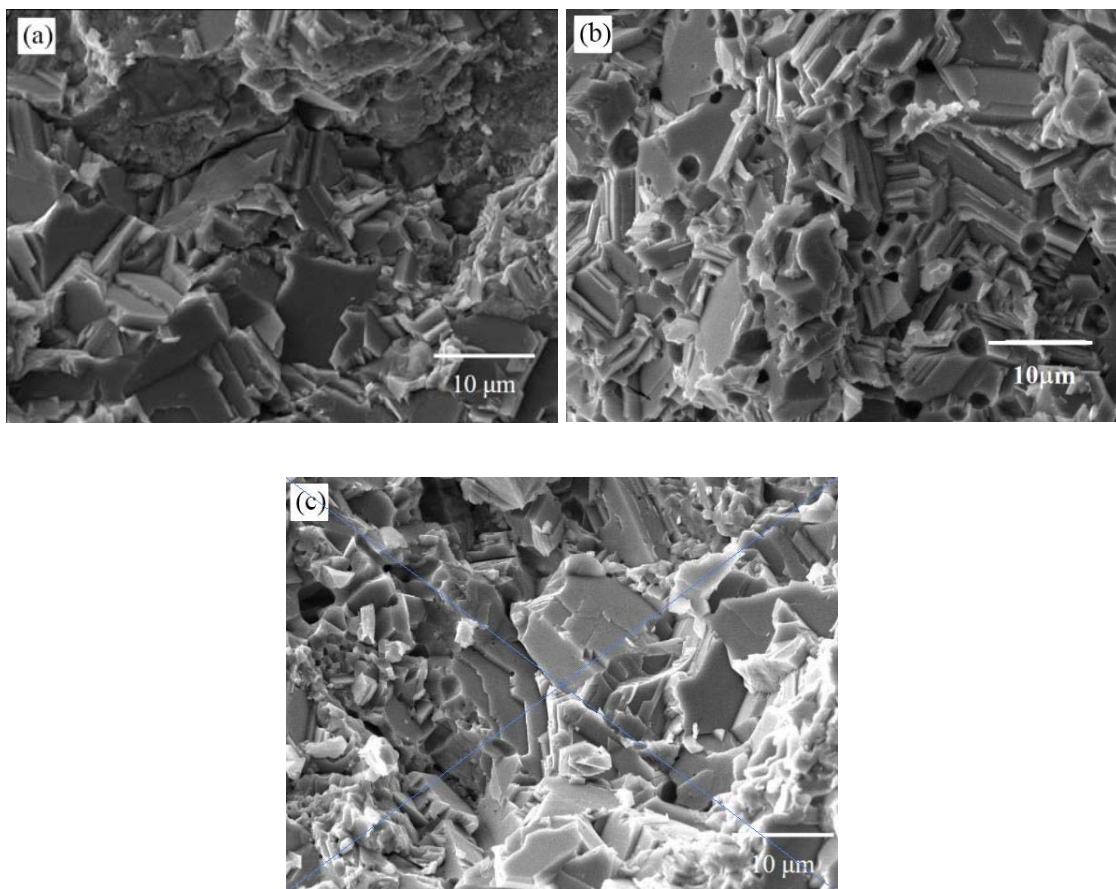


Figure 5.4. SEM images for the cross-sections of $\text{Cu}_{\text{vac-3}}$ sintered with different temperatures: (a) 873 K, (b) 973 K and (c) 1073 K.

5.2.2 Thermoelectric Performance

To explore the thermoelectric performance for samples with different rates of Se evaporation, the σ and S were simultaneously measured and the PF was also evaluated against temperature. As shown in Figure 5.5(a), all the data show an abrupt change at ~ 400 K, which is due to the phase transition from the low-temperature phase to the high-temperature β -Cu₂Se phase. When compared with the samples sintered at lower temperatures, the sample sintered at 1073 K with lower Cu vacancy density exhibited lower σ during heating from 400 K to 800 K, which is attributed to: (1) The simple electron counting rule: the σ is highly associated with the density of Cu vacancy in the sample (A. F. May et al., 2009); (2) Density function theory (DFT) studies proposed by Sun et. al (H. Sun et al., 2017): the increased Cu vacancy density would lower the Fermi level to the edge of valance band near Γ point in reciprocal space, resulting in the increment of carrier concentration; (3) The equation $\sigma = nq_e\mu$: σ increases with the carrier concentration n with the assumption of a constant carrier mobility μ where q_e is the electronic charge. As the sintering condition was shown to affect the microstructure as well as the stoichiometric value of Cu and Se, the thermoelectric performance of samples should also be affected by the variation of Cu vacancy density. To explore the effect of Cu vacancy density on the data repeatability of samples, the σ and S were performed under a thermal cycle. Figures 5.5(a) and (b) show that the sample sintered at 873 K exhibited the smallest variation between the heating and cooling curves among three samples while the one sintered at 1073 K exhibited the largest variation.

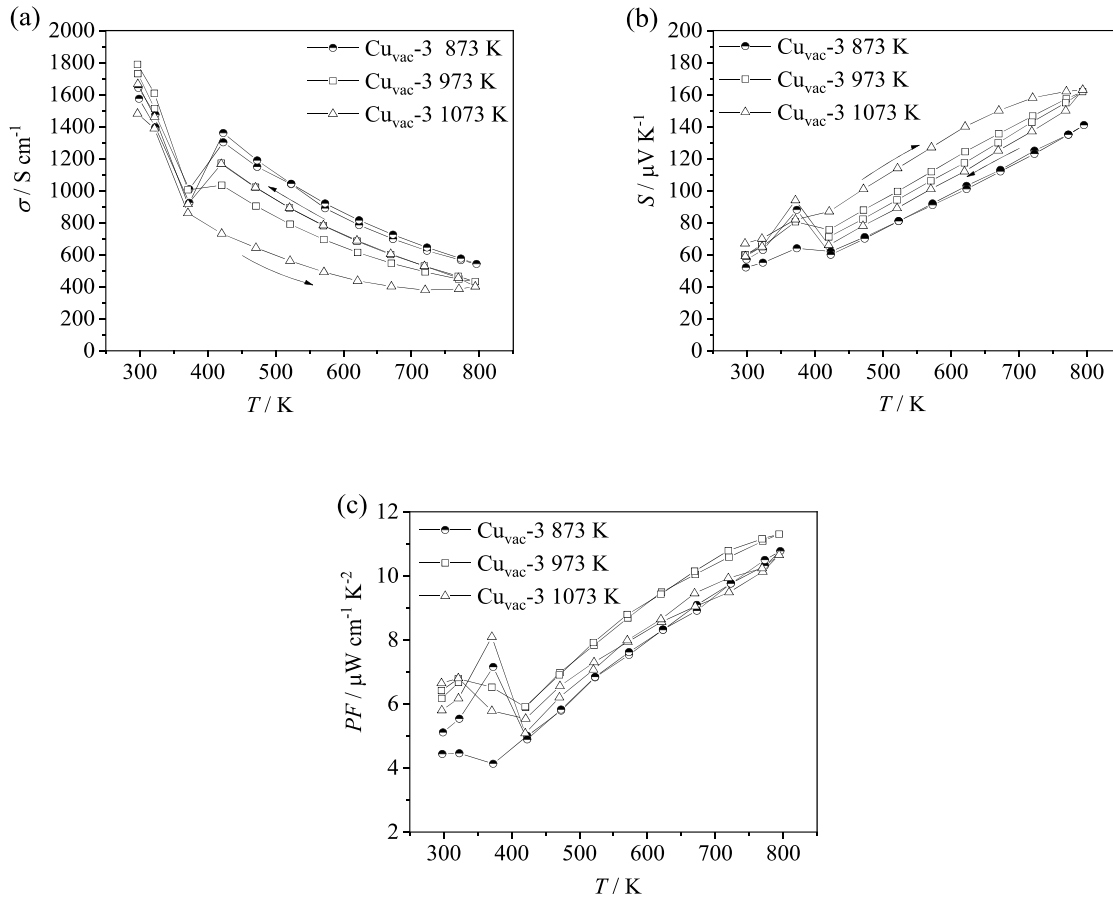


Figure 5.5. Temperature dependence of (a) σ , (b) S and (c) PF for $\text{Cu}_{\text{vac}}\text{-3}$ sintered at different temperatures.

The thermal stability of the $\text{Cu}_{\text{vac}}\text{-3}$ samples was shown to correlate to the rate of Se evaporation such that the lowest rate of Se evaporation due to the lowest sintering temperature would give the best repeatability upon the heating and cooling processes. Besides, the PF was determined for the samples sintered at 873 K, 973 K, and 1073 K, respectively, as shown in Figure 5.5(c). The largest PF of $\sim 11 \mu\text{W m}^{-1} \text{ K}^{-2}$ was found at 800 K for the sample sintered at 973 K. Interestingly, even though the sample sintered at 1073 K did not show good data repeatability on σ and S , the repeatability was good for the PF from 450 K to 800 K.

The cycling performance for D and κ_{tot} of the samples sintered at different sintering temperatures was evaluated and shown in Figure 5.6. Different from the electrical properties, the sample sintered at 1073 K also exhibited good data repeatability for both D and κ_{tot} , which should be attributed to the re-annealing effect. As Se tends to evaporate during the high-temperature sintering process, the composition may not be homogeneous throughout the as-prepared sample such that the first-round measurement of electrical properties show the big variation between the heating and cooling curves. Nevertheless, the sample was heated under high temperature (up to 800 K) for a long period of time during the measurement, which can be regarded as the re-annealing process for the sample that would improve the homogeneity and help achieving the equilibrium. As the measurement of thermal transport properties was the second-round (2nd) measurement, the κ_{tot} could achieve very good repeatability in the thermal cycle for all samples. To verify this point of view, thermal cycling tests were further performed for the sample sintered at 1073 K.

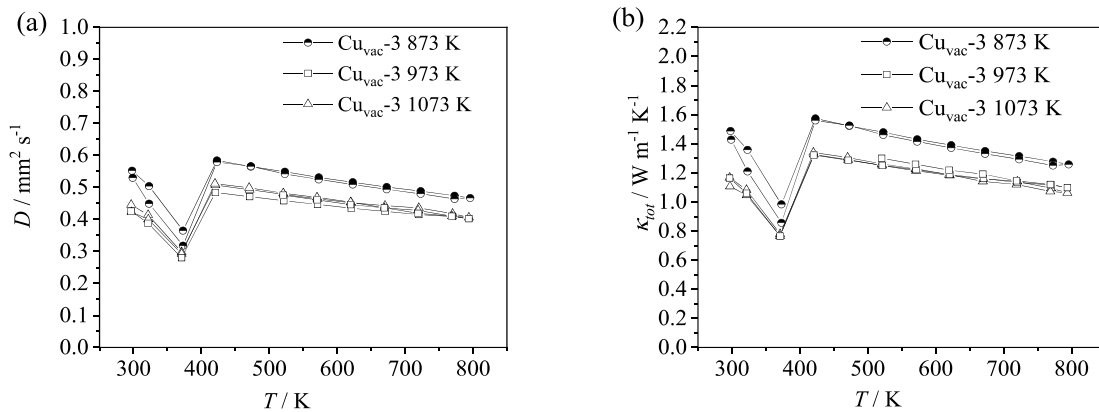


Figure 5.6. Temperature dependence of (a) D and (b) κ_{tot} for $\text{Cu}_{\text{vac}}\text{-3}$ sintered at different temperatures.

Figure 5.7 shows the thermal cycling results for σ and S of the sample sintered at 1073 K. It should be noted that the 2nd test was performed to measure the D , so the tests for σ and S are named as the first-round (1st), the third-round (3rd), and the fourth-round (4th), respectively. It was found that the variations between the heating and cooling curves are getting smaller and smaller by thermal cycling, which should be attributed to the improved chemical uniformity and thermal stability of the samples after repeated annealing processes. Again, the calculated PF data show extremely good repeatability in the 3rd and 4th thermal cycles, which can also be found in Olvera's work (Olvera et al., 2017). According to the definition of zT and SPB model, the good repeatability of PF might not guarantee the stable thermal performance of thermoelectric materials due to the variation of κ_e .

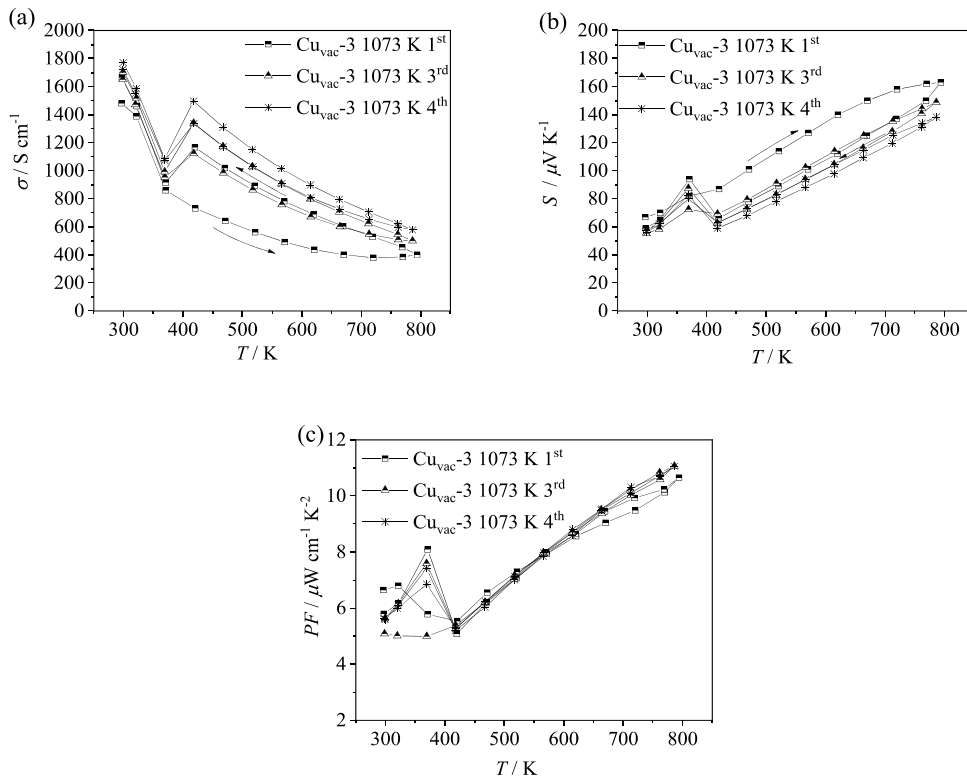


Figure 5.7 Thermal cycling performance for $\text{Cu}_{\text{vac}}\text{-3}$ sintered at 1073 K: (a) σ , (b) S and (c) PF .

The SPB model was adopted to explore the contribution of electronic and lattice parts to the κ_{tot} . As shown in Figure 5.8(a), the samples sintered at lower temperatures have higher κ_e , which is mainly attributed to their higher σ . The trend is just the opposite for the case of κ_l in which the samples sintered at higher temperatures exhibit higher κ_l as shown in Figure 5.8(b).

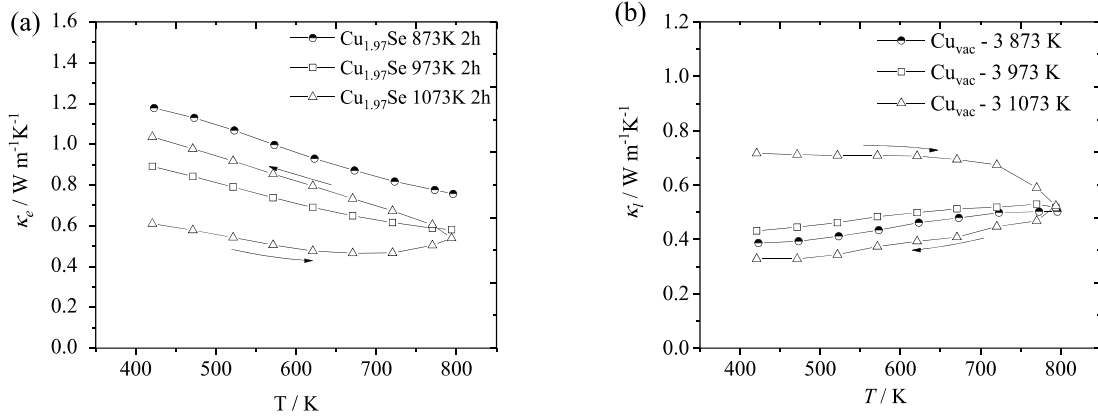


Figure 5.8. Temperature dependence of (a) κ_e and (b) κ_l for Cu_{vac-3} sintered at different temperatures.

This should be due to the enlarged average grain size of the samples sintered at higher temperatures as shown in Figure 5.4, which could significantly promote the phonon propagation and maintain the high κ_l . According to the calculation of the vibrational modes in the phonon density of state, DOS, the heat-carrying capacity would decrease due to the shift of the vibration frequency to a lower value (S. Namsani et al., 2017), so the κ_l would slightly decrease against the temperature. In Figure 5.8(b), the κ_l was found to vary from the normal trend since the material undergoes physical change (the annealing effect). The SPB model seems not to be suitable for the systems under dynamic states (composition change).

The temperature dependent measured zT and the SPB model results of the $\text{Cu}_{\text{vac}}\text{-3}$ sintered at different temperatures are shown in Figure 5.9. The enhanced zT can be realized by increasing the B factor. As shown in Figure 5.9(a), the zT of the samples increased with the testing temperature and the sintering temperature, which is primarily due to the increment of B (higher peak in Figure 5.9(b)) and the reduction of n (reduced Cu vacancy).

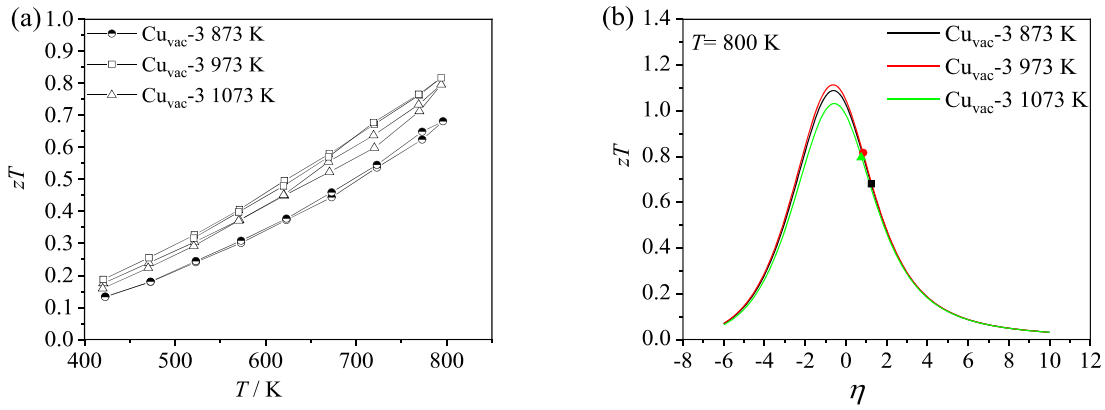


Figure 5.9. (a) Temperature dependence of zT of $\text{Cu}_{\text{vac}}\text{-3}$ sintered at different temperatures, and (b) SPB model results at 800 K with the measured zT of $\text{Cu}_{\text{vac}}\text{-3}$ sintered at different temperatures (represented by solid symbols with the colors corresponding to the curves).

The maximum zT appeared to be 0.817 at 800 K for the samples sintered at 973 K for 2 hours. Besides, all the samples show good repeatability in thermal cycling even for the sample sintered at 1073 K despite its initial variations of σ and S between the heating and cooling curves. Nevertheless, the zT of the sample sintered at 1073 K was slightly lower than that sintered at 973 K, which may be due to the unstable PF data of the sample sintered at 1073 K that was obtained from the 1st cycling test. According to Wiedemann-Franz Law, the large variations of σ would give large deviations of κ_l so as to deduce that the zT curve obtained from the 1st cycling test should not be consistent when compared to the good repeatability of κ_{tot} in the 2nd cycling test.

Due to the difficulty of the simultaneous measurements of electrical properties and thermal properties, the zT data can only be provided from two individual measurements (Figures 5.5 and 5.6).

5.3 Conclusion

The thermal cycling performance for $\text{Cu}_{\text{vac}}\text{-3}$ fabricated using the conventional sintering method has been firstly reported and systematically investigated. The preparation conditions were found to strongly affect the electron transport properties, and eventually the thermoelectric performance due to the evaporation of Se. The samples sintered at 973 K for 2 hours show the optimized zT of 0.817 at 800 K with very good data repeatability in thermal cycling. The results show that the $\text{Cu}_{\text{vac}}\text{-3}$ fabricated using the simple and cost-effective method could also exhibit the excellent repeatability in thermal cycling.

Chapter 6

Vapor Pressure Control of the Conventional Sintering Method in the Fabrication of $\text{Cu}_{1.97}\text{Se}$ Superionic Thermoelectric Material

From Chapters 4 and 5, Cu vacancy and chemical uniformity of the sample is paramount to have data repeatability. Besides, the TGA curve could provide information for thermal stability at a specific atmosphere. The sintering temperature might exceed the temperature at which the sample is unstable due to the thermal dynamic condition (temperature, vapor pressure, etc). Regarding the Se evaporation during the sample fabrication in Chapters 4 and 5, a large temperature difference exists for the chamber, which might be the driving force of Se evaporation. In this chapter, the $\text{Cu}_{\text{vac}}\text{-3}$ sample in a saturated Se vapor pressure environment will be studied and compared to the $\text{Cu}_{\text{vac}}\text{-3}$ sample sintered in an open area at 973 K. The repeatability of the data will also be studied.

6.1 Materials Preparation

$\text{Cu}_{\text{vac}}\text{-3}$ powder was synthesized by the conventional solid-state sintering technique. The starting materials, Cu (99.99%) and Se (99.99%), were used and calculated according to the chemical formula. Then, the mixture was sealed in a quartz crucible and melted at 1453 K for 2 hours and annealed at 973 K for 10 hours. The as-prepared powder was ground into fine powder using an agate mortar, weighed, and pressed into discs under a pressure of 300 MPa. Finally, the discs with a diameter of ~13 mm and a thickness of ~0.7 mm were sintered again at 973 K for 2 hours, and then slowly cooled down to room temperature.

Two sintering setups are adopted for comparisons and shown in Figure 6.1. One of them was to place the samples in the center (isothermal area marked with a red square) of a tube furnace, experiencing the sintering atmosphere and the temperature gradient along the tube, as shown in Figure 6.1(a).

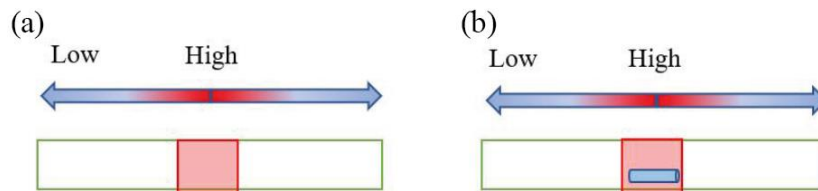


Figure 6.1 The sintering setups for samples in a conventional tube furnace with an isothermal space marked by a red square: (a) samples placed in the isothermal space and exposed to the sintering atmosphere, and (b) samples sealed in a small quartz tube located in the isothermal space (the length of a small quartz tube is within the isothermal space of the tube furnace).

The other setup in Figure 6.1(b) was to place the samples in a small sealed quartz tube with a diameter of 15 mm and a length of ~10 mm located in the isothermal area of the furnace. The samples obtained from the former and latter setups are named as $\text{Cu}_{\text{vac-3}}$ and $\text{Cu}_{\text{vac-3A}}$, respectively. The control experiment was designed to avoid the introduction of other factors such as the variables of sintering temperature and time. With the conventional sintering method, no external factors such as external electric field (in SPS method) and external force (in HPS method) are required to take into account.

6.2 Results and Discussion

6.2.1 Microstructural Properties

Figure 6.2 shows the PXRD patterns for the $\text{Cu}_{\text{vac-3}}$ samples sintered at 873 K in the tube furnace. The patterns of the $\text{Cu}_{\text{vac-3}}$ samples were collected at 323 K, 373 K, 423 K, and 473 K, respectively, with a specific scanning step of 0.01° in the range of $20\text{-}80^\circ$. As shown in Figure 6.2, the room-temperature monoclinic phase for $\text{Cu}_{\text{vac-3}}$ existed until 423 K, which was proved by the diffraction peaks at $\sim 40^\circ$ in the high-temperature XRD results. When the temperature was higher than 423 K, the sample turned into the cubic phase with the disappearance of peaks at $\sim 40^\circ$.

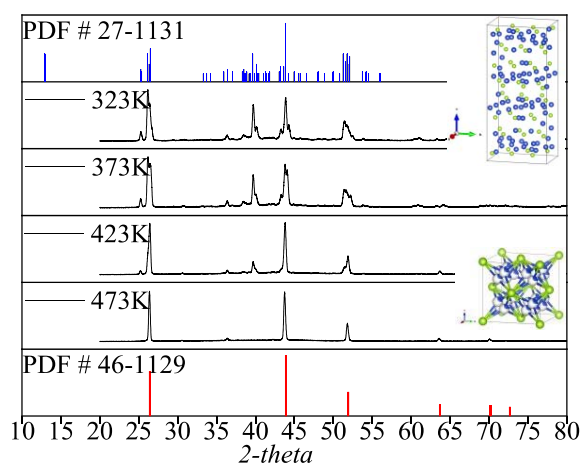


Figure 6.2 PXRD patterns for $\text{Cu}_{\text{vac-3}}$ sintered at 873 K in a tube furnace. The data was collected from 323 K to 473 K per 50 K in vacuum. (Blue column bars show the standard PDF card #27-1131 diffraction peak sites for the low-temperature $\alpha\text{-Cu}_2\text{Se}$ phase; Red column bars show the standard PDF card #46-1129 diffraction peak sites for the high-temperature $\beta\text{-Cu}_2\text{Se}$ phase).

To explore the difference of the thermal stability for $\text{Cu}_{\text{vac-3}}$ with different sintering environment, TGA measurement was performed under one atmosphere with N_2 flow. The weight loss data was obtained for all samples from room temperature to 1073 K at a speed of 10 K min^{-1}

and the continued isothermal section at 1073 K for 1 hour. As shown in Figure 6.3, $\text{Cu}_{\text{vac}}\text{-3A}$ shows an abrupt drop at around 800 K compared with $\text{Cu}_{\text{vac}}\text{-3}$, which is due to the different environment during the sintering process. To well characterize the thermal dynamic behavior of $\text{Cu}_{\text{vac}}\text{-3}$, its powder from ingot was also measured and the data was shown together in Figure 6.3.

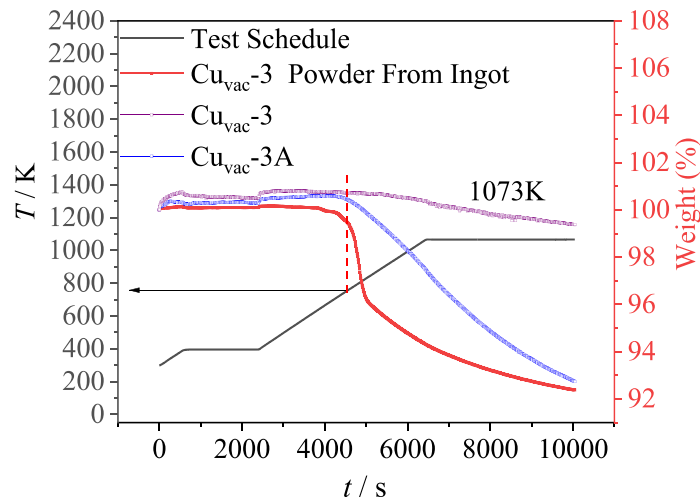


Figure 6.3 TGA curves for weight losses of the $\text{Cu}_{\text{vac}}\text{-3}$ powder from ingot (red line), the $\text{Cu}_{\text{vac}}\text{-3}$ (blue line) and $\text{Cu}_{\text{vac}}\text{-3A}$ (purple line) bulk samples.

For the $\text{Cu}_{\text{vac}}\text{-3A}$ sample sintered in the isothermal space, the evaporation of Se in a limited space can be saturated and even terminated. While for $\text{Cu}_{\text{vac}}\text{-3}$ powder, the origin of Se evaporation comes from the temperature and pressure gradients along the tube furnace, which was verified by the red TGA curve in Figure 6.3. The Se evaporation of $\text{Cu}_{\text{vac}}\text{-3}$ powder was severe due to the large surface area. The turning point for the red curve represents the unstable temperature of the Cu-Se system. When comparing the $\text{Cu}_{\text{vac}}\text{-3}$ and $\text{Cu}_{\text{vac}}\text{-3A}$ with $\text{Cu}_{\text{vac}}\text{-3}$ powder, the huge difference can be observed and explained as follows: $\text{Cu}_{\text{vac}}\text{-3}$ has been experienced the Se evaporation in the sintering process at 973 K in a tube furnace according to the red TGA curve. The 2-hour dwelling

time enabled the sample to undergo severe Se evaporation, and forced the real composition of $\text{Cu}_{\text{vac}}\text{-3}$ shift towards Cu_2Se . The new Cu-Se system becomes more stable due to the reduced Cu vacancy, thus exhibiting a higher turning point as shown in the violet TGA curve in Figure 6.3. For $\text{Cu}_{\text{vac}}\text{-3A}$, the evaporation of Se was suppressed due to the specific sintering setup. Therefore, the evaporation level is between that of powder and $\text{Cu}_{\text{vac}}\text{-3}$, which can be verified from the PXRD and refinement results in the following section.

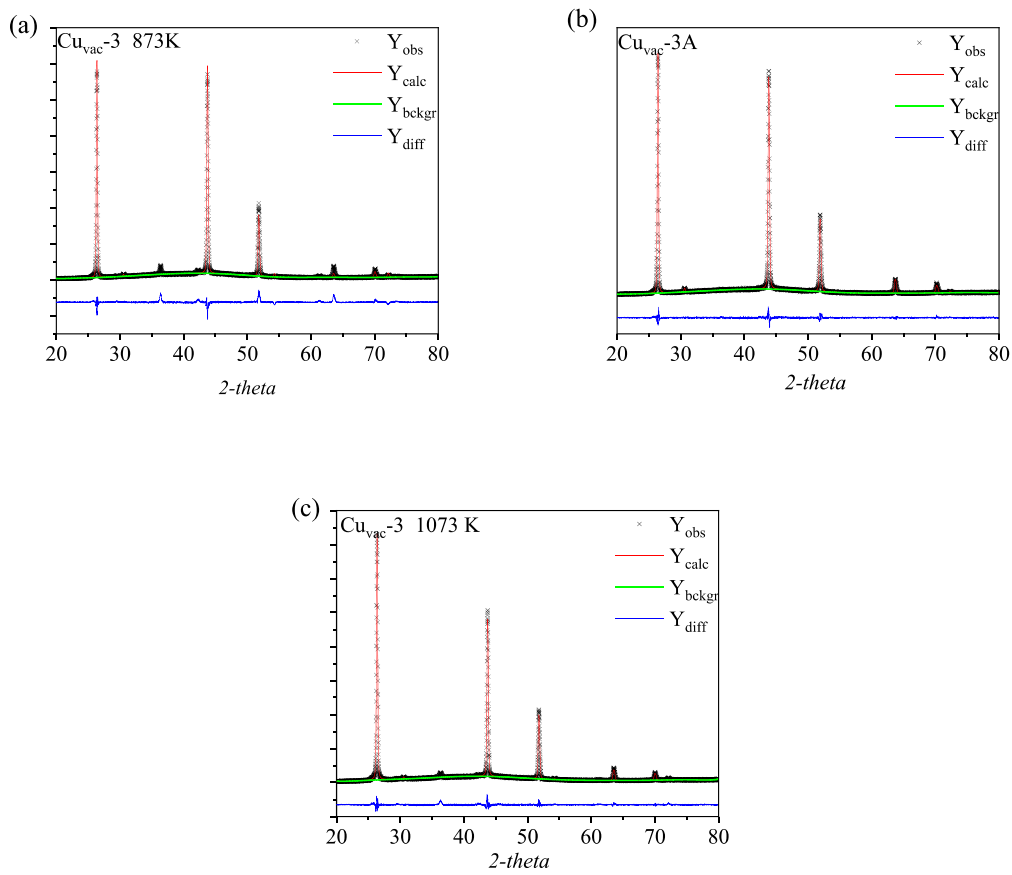


Figure 6.4 Rietveld refinement results of the high-temperature PXRD by using GSAS software.

To explore the effect of sintering condition on the microstructural properties, high-temperature XRD patterns were collected and refined (Figure 6.4). As can be seen in Table 6.1, samples sintered in a long quartz tube show small lattice constant and with higher sintering temperature, the lattice constant increase due to the evaporation of Se. This can also be proven by comparing the diffraction peak (311) from different samples as shown in Figure 6.5(b). In Figure 6.5(b), the Cu_{vac}-3A owns the (311) peaks with the largest *2-theta* angle, which can be explained to own the smallest lattice constant compared with samples sintered at conventional tube furnace (Table 6.1). The highly suppressed Se evaporation might be due to the saturated Se vapor in the small sealed quartz tube, which maintained a high level of Cu vacancy.

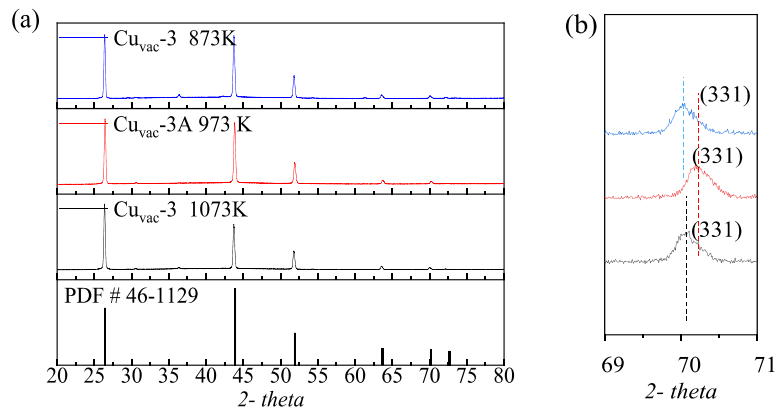


Figure 6.5. High-temperature PXRD patterns for Cu_{vac}-3 sintered at 873 K and 1073 K in a tube furnace and Cu_{vac}-3A sintered at 973K. The black column bars show the standard PDF card #46-1129 diffraction peak sites for the high-temperature β -Cu₂Se phase.

Table 6.1 Lattice parameters derived from the XRD patterns for Cu_{vac}-3 sintered at 873 K and 1073 K, and Cu_{vac}-3A.

samples	Lattice parameters		R-factors		
	a (Å)	$Vol(\text{Å}^3)$	χ^2	$R_p(\%)$	$R_{wp}(\%)$
Cu _{vac} -3-873K	5.853	200.597	3.27	9.35	13.88

Cu _{vac} -3A	5.845	199.707	1.25	6.16	8.58
Cu _{vac} -3-1073K	5.859	201.155	1.81	7.12	10.17

Figure 6.6 shows the morphology of Cu_{vac}-3A. The grain size is not uniform with the size of around 1-2 μm . It is reported that the density of samples prepared using the SPS and HPS techniques could reach over 97% of the theoretical density. It was found that the density of samples prepared in the present study could also reach 94% – 95% of the theoretical value, which also shows that the conventional sintering method could also offer good sintering conditions for the materials. This is largely due to the metallic bonding between Cu and Se, which will be proved by the decreasing σ against temperature as shown in the next section.

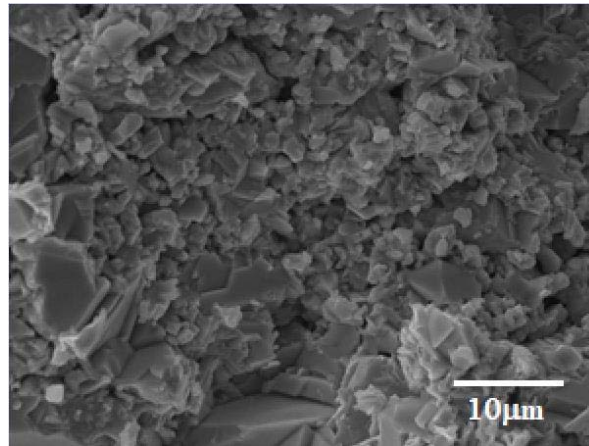


Figure 6.6 SEM image for the cross-sections of Cu_{vac}-3A.

6.2.3 Thermoelectric Performance

For the curves of σ , as shown in Figure 6.7(a), Cu_{vac}-3 and Cu_{vac}-3A show a large difference over the whole temperature range in the measurement. The samples sintered in a sealed small quartz tube showed higher σ during the elevating temperature range from 400 K to 800 K, when compared with the ones exposed to the sintering atmosphere in a tube furnace. According to our

previous study about the relationship between Cu vacancy concentration and σ , a higher Cu vacancy concentration would maintain higher n , thus larger σ would be retained. As the only difference of sintering conditions between two samples is the sintering circumstance, the result verified that the sintering in a closed space and isothermal space can highly suppress the Se evaporation. For S , the $\text{Cu}_{\text{vac}}\text{-3A}$ showed lower values compared to $\text{Cu}_{\text{vac}}\text{-3}$, which is highly related to the high Cu vacancy concentration due to the suppressed Se evaporation.

As shown in both Figures 6.7(a) and 6.7(b), the sample sintered in the sealed quartz tube showed the excellent data repeatability in thermal cycling, which is probably due to the homogeneous composition across the sample benefited from the suppressed evaporation of Se.

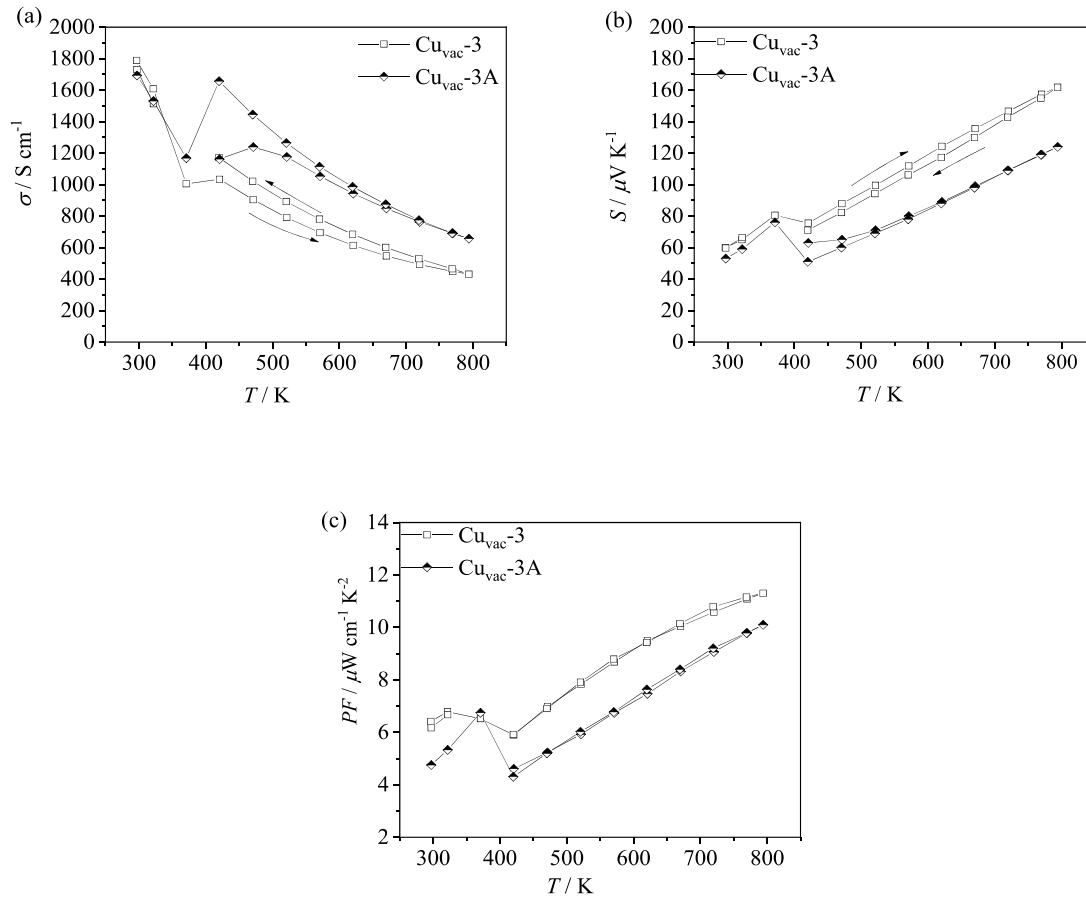


Figure 6.7. Temperature dependence of (a) σ , (b) S , and (c) PF for $\text{Cu}_{\text{vac}}\text{-3}$ and $\text{Cu}_{\text{vac}}\text{-3A}$, respectively.

As shown in Figure 6.7(c), the values of PF for samples sintered at 973 K increased with temperature from 400 K. It has been found that both the samples sintered in a tube and sealed quartz tube show small variations of PF curves obtained in the thermal cycling. However, the significant drop of PF values can be detected for $\text{Cu}_{\text{vac}}\text{-3A}$, which might be due to the high Cu vacancy concentration. The D and κ_{tot} of the samples sintered at 973 K are shown in Figure 6.8. It should be noted that the D of $\text{Cu}_{\text{vac}}\text{-3A}$ was found to be larger than that of $\text{Cu}_{\text{vac}}\text{-3}$, which is due to the higher n of $\text{Cu}_{\text{vac}}\text{-3A}$.

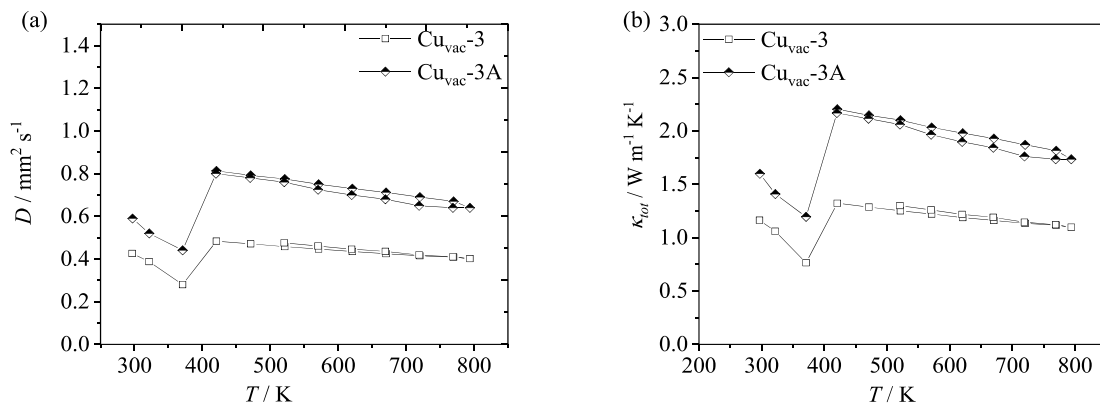


Figure 6.8 Temperature dependence of (a) D , and (b) κ_{tot} for $\text{Cu}_{\text{vac}}\text{-3}$ and $\text{Cu}_{\text{vac}}\text{-3A}$ sintered at 973 K.

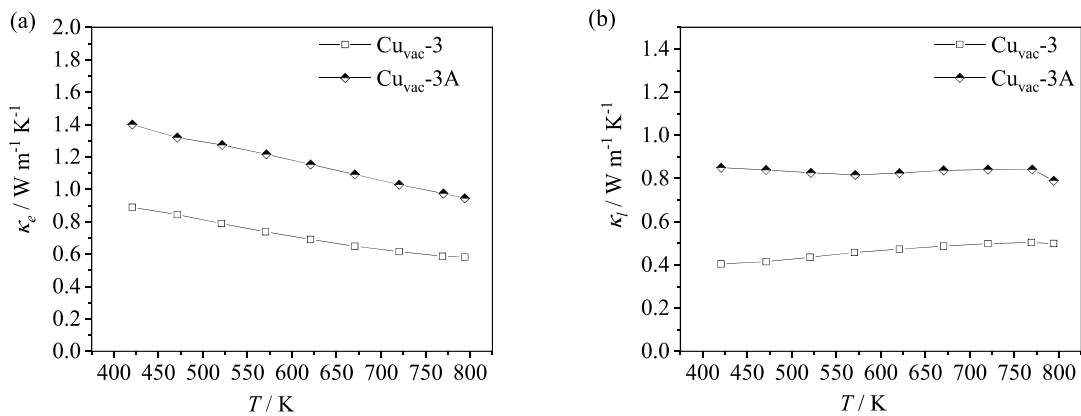


Figure 6.9 Temperature dependence of (a) κ_e , and (b) κ_l for $\text{Cu}_{\text{vac}}\text{-3}$ and $\text{Cu}_{\text{vac}}\text{-3A}$ sintered at 973K

To explore the contribution of electronic and lattice parts to the κ_{tot} , the SPB model in Chapter 3 was adopted and the results are shown in Figure 6.9. The κ_e showed a decreasing tendency against the testing temperature, while the samples sintered in a sealed quartz tube exhibited higher κ_e , which is mainly attributed to the higher n . Moreover, the κ_l of Cu_{vac}-3 was also smaller, which might be due to its smaller average grain size.

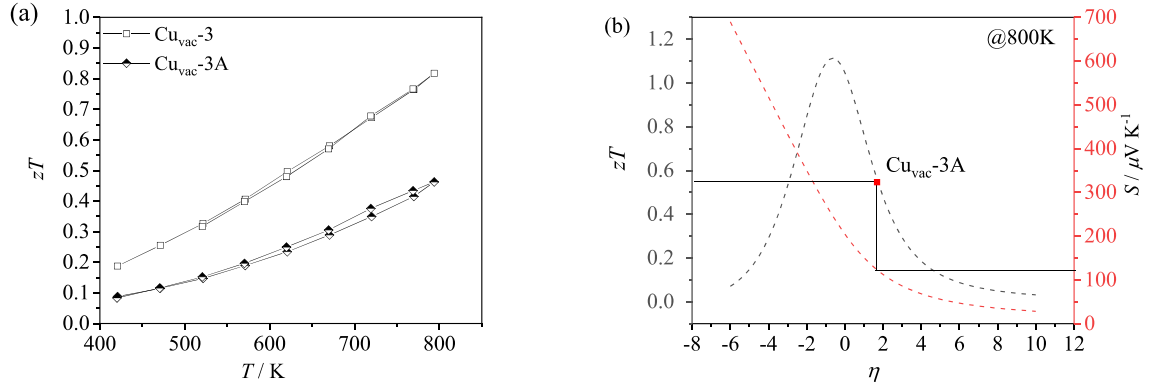


Figure 6.10 (a) Temperature dependence of zT for Cu_{vac}-3 and Cu_{vac}-3A sintered at 973 K, and (b) SPB model results at 800 K (black dash line for zT and red dashed line for S) with the measured zT of Cu_{vac}-3A (represented by a square symbol).

The overall zT of Cu_{vac}-3 and Cu_{vac}-3A is shown in Figure 6.10. The peak values of zT at 800 K were 0.8 and 0.45 for Cu_{vac}-3 and Cu_{vac}-3A sintered at 973 K, respectively. The huge difference of zT is mainly due to the higher n for Cu_{vac}-3A that is originated from the Se vapor condition. It should be noted that the composition control is critical for thermoelectric transport (electron transport and phonon transport). Thus, an effective sintering method to synthesize densified samples with the minimal variation of the composition is highly desired.

6.3 Conclusion

The $\text{Cu}_{1.97}\text{Se}$ fabricated using the conventional sintering method has been investigated in terms of the sintering atmosphere. The preparation conditions strongly affect the stoichiometric ratio of Cu:Se and electron transport and eventually the thermoelectric performance. It was found that the samples sintered in an isothermal space could strongly suppress the evaporation of Se. Though the experimental zT value could only reach 0.45 at 800 K, which is smaller than that of the sample exposed to the sintering atmosphere in a long quartz tube. Moreover, the merit of bulk sample fabrication in an isothermal area could maintain the uniformity of the sample, which is beneficial for samples having precise controlling of chemical composition.

Chapter 7

Stoichiometric $\text{Cu}_{1.97}\text{In}_x\text{Se}$ Fabricated Using the Conventional Sintering Method

The previous studies have proved that the conventional sintering method could be employed to synthesize the materials with reasonably good thermoelectric performance. Based on the studies of effects of Cu vacancy on Cu_{2-x}Se in Chapter 4 and sintering parameter on $\text{Cu}_{1.97}\text{Se}$ in Chapter 5, the doping technique is utilized for the Cu_{2-x}Se system taking into account of effective Cu vacancy and appropriate sintering temperature in this Chapter. The sintering temperature was selected as 973 K. The sintering atmosphere was investigated by comparing the thermoelectric performance of the samples sintered in a sealed quartz tube and an open area in the tube furnace, respectively. In was chosen as the doping element due to its heavy atomic weight (114.8u) when compared to Cu (63.5u). It is anticipated that the atomic weight difference would contribute to the suppression of phonon transport, resulting in the reduction of the κ_l . The zT will then be enhanced due to the reduction of the κ_{tot} . Nevertheless, due to the large ionic radius of In, its solubility into the Cu sites should be limited such that a new phase CuInSe_2 (CIS) might be introduced.

7.1 Materials Preparation

The starting materials, Cu (99.9%), Se (99.99%) and In (99.99%), were weighed along with the composition and mixed in a carbon-coated quartz crucible and melted at 1453 K for 2 hours in the tube furnace followed with the 10-hour annealing at 973 K and natural cooling. Then, the as-prepared powder was milled into fine powder using an agate mortar, weighed and pressed into

discs under a pressure of 300 MPa. Finally, the discs with a diameter of ~13 mm and a thickness of ~0.6 mm were again sealed in a quartz tube with a diameter of 15 mm and a length of ~10 mm. To investigate the effect of doping element In on the thermoelectric performance, the samples prepared using the setup shown in Figure 6.1(b) are named as Cu_{vac}-3A-In with regard to Cu_{vac}-3A

7.2 Results and Discussion

7.2.1 Microstructural Properties

Figure 7.1 shows the PXRD patterns of the conventional sintered Cu_{vac}-3A-In, which displays the main pattern of a single-phase material that is identical to the low-temperature monoclinic Cu-Se phase. This indicates that the In atoms can enter the Cu_{vac}-3A phase even with a relatively large atomic radius ($r_{\text{Cu}} = 128$ pm while $r_{\text{In}} = 220$ pm). The primary phase is identified as the α -Cu₂Se phase with a comparison to the standard XRD card (PDF #027-1131). Except for those diffraction peaks originated from the low-temperature α -Cu₂Se phase, the impurity peaks belong to CuInSe₂ (compared to the standard XRD card PDF #40-1487). Besides, Figure 7.1 shows the PXRD pattern of Cu_{vac}-3A-In at 473 K, which is consistent with the standard card PDF#46-1129. To evaluate the influence of the In doping on the Cu-Se structure, GSAS software was applied to analyze the phase structure and obtain the refinement results as shown in Figure 7.2 and Table 7.1, respectively. The cell volume was found to enlarge from 199.707 Å³ to 201.93 Å³ due to the substitution of In into the Cu lattice.

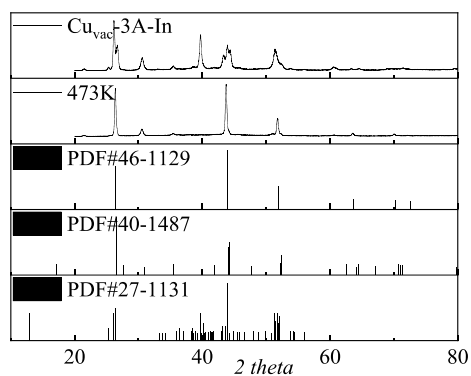


Figure 7.1 PXRd patterns for $\text{Cu}_{\text{vac}}\text{-3A-In}$ at room temperature and 473 K.

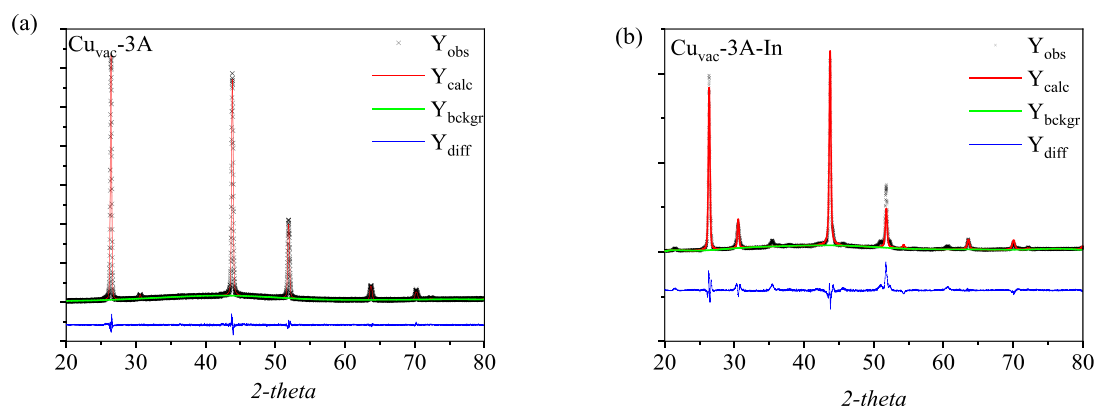


Figure 7.2 Rietveld refinements of high-temperature PXRd profiles of (a) $\text{Cu}_{\text{vac}}\text{-3A}$ and (b) $\text{Cu}_{\text{vac}}\text{-3A-In}$ using GSAS software.

Table 7.1 Rietveld analysis of PXRd results for $\text{Cu}_{\text{vac}}\text{-3A}$ and $\text{Cu}_{\text{vac}}\text{-3A-In}$.

Samples	Lattice parameters		R-factors		
	a (Å)	Vol (Å ³)	χ^2	R_p (%)	R_{wp} (%)
$\text{Cu}_{\text{vac}}\text{-3A}$	5.845	199.707	1.25	6.16	8.58
$\text{Cu}_{\text{vac}}\text{-3A-In}$	5.867	201.930	5.76	14.33	19.4

When compared the TGA results of $\text{Cu}_{\text{vac}}\text{-3A-In}$ with $\text{Cu}_{\text{vac}}\text{-3A}$, the difference of the turning point of weight loss was detected (Figure 7.3). With the doping of In, the thermal stability of $\text{Cu}_{\text{vac}}\text{-3A-In}$ can be further enhanced up to 1073 K. This is absolutely beneficial for the application of Cu-Se system. The enhanced thermal stability is highly related to the introduction of In in the Cu-Se system, which is due to the existence of CuInSe phase (A. A. Oliva et al., 2017).

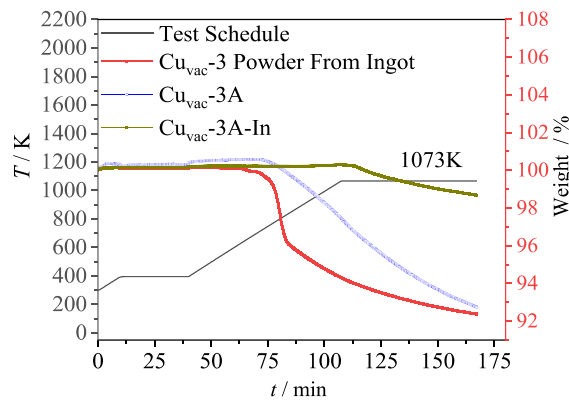


Figure 7.3. TGA data for weight losses of the $\text{Cu}_{\text{vac}}\text{-3}$ powder from ingot (red line), the $\text{Cu}_{\text{vac}}\text{-3A}$ (blue line) and $\text{Cu}_{\text{vac}}\text{-3A-In}$ (green line) bulk samples.

Figure 7.4 shows the SEM images of $\text{Cu}_{\text{vac}}\text{-3A-In}$ fabricated using the conventional sintering method. The grain size for the doped samples was around 2-3 μm . The addition of In into the $\text{Cu}_{\text{vac}}\text{-3A}$ system seems not to influence the sintering behavior and morphology significantly. The layered structure was detected as the main phase of Cu_{2-x}Se , while some small irregular grains existed. According to Olvera's work (A. A. Olvera et al., 2017), the agglomerations without distinct grain shape should belong to the CuInSe_2 phase that is difficult to be distinguished due to the similar

crystal structure of Cu_2Se . The impurity phase would affect the thermoelectric performance, which will be discussed in the following sections.

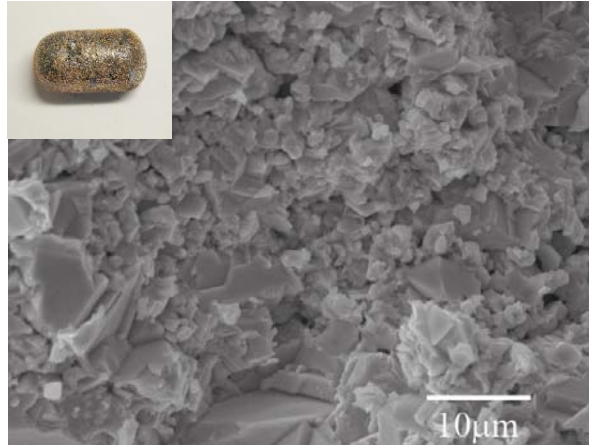


Figure 7.4 SEM image for the cross sections of $\text{Cu}_{\text{vac}}\text{-3A-In}$, and (inset) the picture of the as-prepared ingot.

7.2.2 Thermoelectric Performance

To investigate the influence of In dopant on the performance of $\text{Cu}_{\text{vac}}\text{-3A-In}$, the thermoelectric properties were measured and shown in Figure 7.5. Figure 7.5(a) shows the σ of $\text{Cu}_{\text{vac}}\text{-3A-In}$ with respect to the testing temperature, in which a very high σ of $1.47 \times 10^3 \text{ S cm}^{-1}$ was observed at room temperature. This value is larger than that of the SPS-assisted ones (Liu et al., 2012), and even double that of the nanostructured Cu_2Se (Lei et al., 2016) reported recently. According to the literature (Lei et al., 2016), σ strongly depends on the grain size of polycrystalline Cu_2Se . Specifically, both very large and nanostructured grain sizes would deteriorate the σ .

Figure 7.5(b) shows the S of $\text{Cu}_{\text{vac}}\text{-3A-In}$ as a function of temperature, in which the positive S indicates that the polycrystalline $\text{Cu}_{\text{vac}}\text{-3A-In}$ is the p-type material with holes as the majority

carriers. The S of $\text{Cu}_{\text{vac}}\text{-3A-In}$ increased with temperature and reached to the maximum value of $150 \mu\text{V K}^{-1}$ at 973 K , which is comparable to the reported values of the SPS-assisted samples. As shown in Figure 7.5(c), the existence of In does not only enhance the S , but also improve the PF . The maximum PF of $\text{Cu}_{\text{vac}}\text{-3A-In}$ was $\sim 10.7 \mu\text{W m}^{-1} \text{ K}^{-2}$. A similar phenomenon has also been observed previously (Tristan et al., 2014).

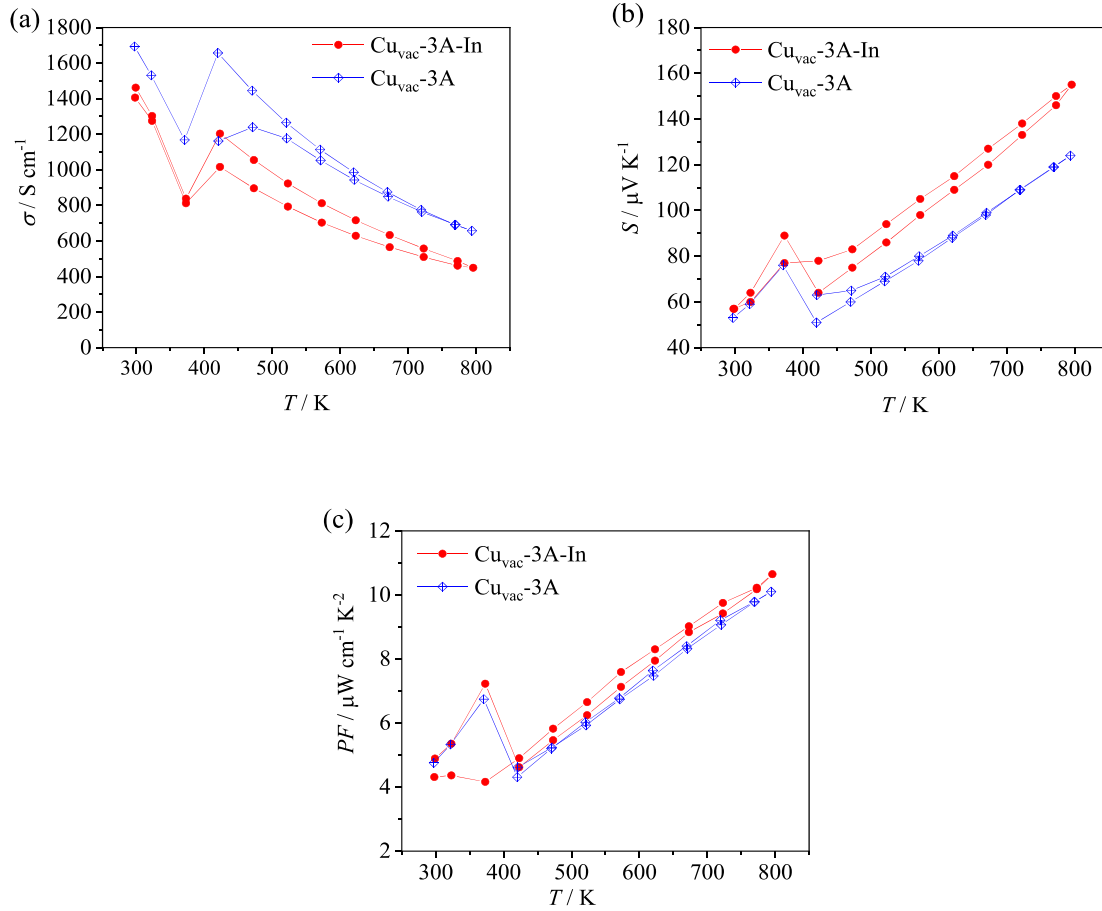


Figure 7.5 Temperature dependence of (a) σ , (b) S and (c) PF for $\text{Cu}_{\text{vac}}\text{-3A-In}$ and $\text{Cu}_{\text{vac}}\text{-3A}$.

To comprehend the contribution of low κ_{tot} in the thermoelectric performance, the κ_e and the κ_l are considered using the equation $\kappa_{\text{tot}} = \kappa_e + \kappa_l$. For the high-temperature $\beta\text{-Cu}_2\text{Se}$ phase, a

combination of an isolated Se atom and a group of three Cu atoms dominates the crystal structure (Tristan et al., 2014). With the highly ordered Se atoms stacked in a close-packed configuration, Cu atoms usually occupy the center of the Se tetrahedrons. Moreover, the total occupancy of the Cu sites is around 1, which means that no Cu vacancy is remained for other In atoms if the CuInSe₂ phase was formed. Thus, for Cu_{vac}-3A-In, Cu might dissolve out from the Cu-Se system. The inset of Figure 7.4 shows the proof that Cu dissolved out from the surface of Cu_{vac}-3A-In ingot. On the other hand, at high temperatures, in most of the tetrahedrons, the superionic Cu ions would drift from the center to one of the triangular faces or the edge of the tetrahedron. This would give spaces to allow In to fill into those center sites.

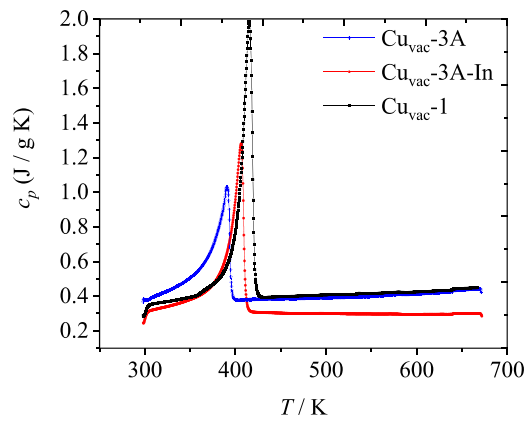


Figure 7.6 Temperature dependence of the specific heat capacity, c_p , for Cu_{vac}-1, Cu_{vac}-3A and Cu_{vac}-3A-In.

The temperature dependences of c_p for Cu_{vac}-3A and Cu_{vac}-3A-In measured using differential calorimetry upon heating (2 K/min) are shown in Figure 7.6. The phase transition temperature can be seen at ~420 K, and no other transition peaks are observed near this temperature. Compared to Cu_{vac}-3A, In-doped Cu_{vac}-3A shows lower c_p for high temperature phase, presenting the strong softening effect (A. A. Olvera et al., 2017). According to Olvera, a decrease in the heat capacity

of a material corresponds to the reduction in the degrees of freedom of atomic motions within its structure. This implies that the diffusivity of Cu^+ ions within the crystal lattice decreases upon incorporation.

As shown in Figure 7.7(a), $\text{Cu}_{2-x}\text{In}_x\text{Se}$ shows a dramatic drop of D when compared to $\text{Cu}_{\text{vac}}\text{-3A}$ (half κ_{tot} of the undoped one). This phenomenon is remarkable particularly when the doping amount of In was only 3%, which should be mainly attributed to the heavy nature of In. In Figure

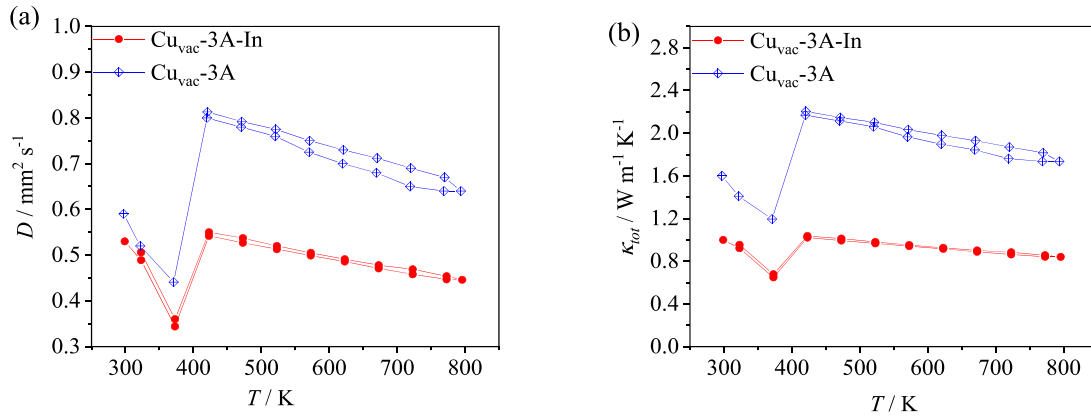


Figure 7.7. Temperature dependence of (a) D and (b) κ_{tot} for $\text{Cu}_{\text{vac}}\text{-3A}$ and doped $\text{Cu}_{\text{vac}}\text{-3A-In}$.

7.7(b), a large leaping of the κ_{tot} is found at ~ 400 K for $\text{Cu}_{1.97}\text{Se}$, indicating its phase transition point. This shows no significant difference from other SPS-assisted bulk Cu_2Se samples. Compared to $\text{Cu}_{\text{vac}}\text{-3A}$, $\text{Cu}_{1.97}\text{In}_x\text{Se}$ has a lower κ_{tot} in which the minimum value could reach ~ 0.8 W/mK. The ultralow κ_{tot} phenomenon is strongly correlated to the doping of In. When compared with Cu, In is much heavier so that its existence would effectively favor the phonon scattering by mass-difference impurity scattering. Besides, the doping amount of In is less than 5% such that the morphological influence might be limited. Thus, the κ_l should be evaluated to help further analyzing the doping effect of In on the Cu-Se system. By using the SPB model, the κ_l was calculated and the results are shown in Figure 7.8(b). As can be seen, the κ_l was highly suppressed

with the existence of In, which could be attributed to the softening effect of In to the Cu-Se system, resulting in decreasing the c_p significantly. A similar effect was reported for the materials fabricated using the high-energy ball milling method (A. A. Olvera et al., 2017).

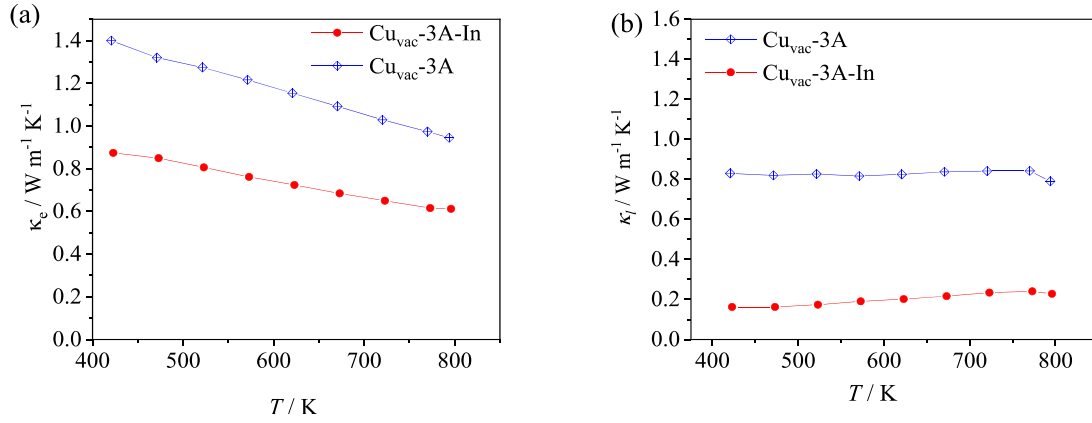


Figure 7.8 Temperature dependence of calculated (a) κ_e , and (b) κ_l for Cu_{vac}-3A and In-doped Cu_{vac}-3A-In.

According to Namsani's calculation, the phonon mean free path of Cu₂Se, λ_0 , ranges from 1.44 Å to 1.06 Å in the temperature range of 500 – 1000 K, which is comparable to the interatomic distance of the Cu-Se system (S. Namsani et al., 2017). Thus, the introduction of In induced the difference of atomic weight so as to impede the lattice vibration to further reinforce the scattering progress. The combined effect of reduced n and enlarged atomic weight difference could reduce the κ_{tot} in a much effective way when compared to the nanostructured mechanism (focused on mid/long wave phonon scattering by introducing nanoparticles).

Figure 7.9(a) shows the temperature dependence of zT of Cu_{vac}-3A and In-doped Cu_{vac}-3A-In samples. Owing to the low κ_{tot} with the doping of In, the maximum zT of 1.0 was obtained at 800 K for Cu_{vac}-3A-In. The theoretical zT of In-doped Cu₂Se could reach further up to 1.8 at 800 K

with the low κ_l and enhanced B as shown in Figure 7.9(b). The experimental zT value for $\text{Cu}_{\text{vac}}\text{-3A-In}$ locates at the higher η side, which means the reduced n is needed for obtaining the optimized zT .

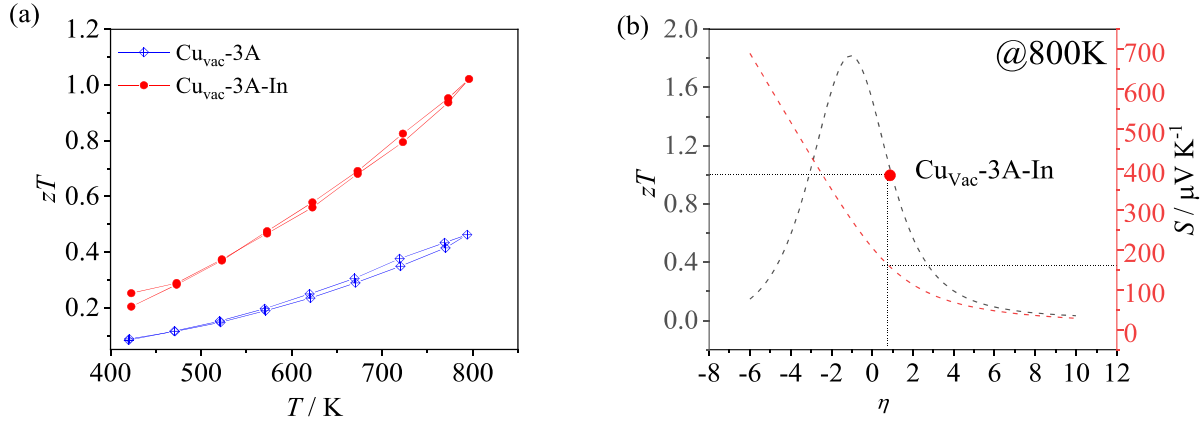


Figure 7.9. (a) Temperature dependence of zT for $\text{Cu}_{\text{vac}}\text{-3A}$ and $\text{Cu}_{\text{vac}}\text{-3A-In}$, and (b) SPB model results at 800 K (black dash line for zT and red dashed line for S) with the measured zT of $\text{Cu}_{\text{vac}}\text{-3A-In}$ (represented by a circle symbol).

7.3 Conclusion

The work on the conventional sintered $\text{Cu}_{\text{vac}}\text{-3A-In}$ suggests that the simple solid-state sintering method cannot only develop promising bulk materials with superior thermoelectric performance, but also possess the promising potential for cost-effective commercialization. It is remarkable that a small amount of In dopant could enhance the thermoelectric performance significantly by introducing interstitial atoms, causing the lattice distortion and inducing the low κ_l . The κ_{tot} of $\text{Cu}_{\text{vac}}\text{-3A-In}$ (0.8 W/mK) was ~ 2 times lower than that of undoped $\text{Cu}_{\text{vac}}\text{-3A}$ (~ 1.9 W/mK), contributing to the high zT of $\text{Cu}_{\text{vac}}\text{-3A-In}$ (~ 1) at 800 K.

Chapter 8

Future Work

As studied in previous Chapters, the Cu chalcogenide-based thermoelectric materials can be fabricated using a conventional sintering method if the sintering parameters (temperature, dwelling time, vapor pressure) are selected carefully. TGA is an instructive technique to provide the information of the maximum working temperature of the thermoelectric materials. Although the sintering temperature is not a significant factor to help obtaining densified samples, the selection of sintering temperature should be considered carefully regarding the unstable temperature obtained from the TGA results. If the materials were unable to be sintered at low temperature, higher sintering temperature is necessary and the vapor control would become important to control the composition. All the aforementioned factors could highly favor the data repeatability and thermal cycling performance.

Besides, the thermal stability can be enhanced by doping engineering, which is beneficial for thermoelectric materials in high-temperature applications. It was found that with the In doping, the Cu-Se system can be thermally stable up to 973 K that is almost 200 K higher than the undoped CuSe. The thermoelectric performance could be tried to enhance based on the confirmed thermal stability and cycling performance of materials. From the present work, the substitution of heavy atoms could reduce the κ_l effectively and enhance the B based on the prediction of SPB model. Thus, it is possible to further enhance the zT if the doping efficiency can be optimized. The PF will also vary when the κ_l is reduced. To further enhance the thermoelectric performance particularly in terms of thermal stability and data repeatability of the materials, co-doping will be the possible

mean to compensate the loss of PF as well as suppress the phonon propagation. Thus, one of the future work is to explore the feasibility of coexistence of In and other element in the Cu-Se system.

Bibliography

A. A. Olvera, N. A. Moroz, P. Sahoo, P. Ren, T. P. Bailey, A. A. Page, C. Uher and P. F. P. Poudeu. Partial indium solubility induces chemical stability and colossal thermoelectric figure of merit in Cu_2Se . *Energy Environ. Sci.*, 10:1668-1676, 2017.

A. L. N. Stevels, F. Jellinek. Phase transitions in copper chalcogenides: I. The copper-selenium system. *Recl, Trav. Chim. Pays-Bas-J. Roy. Neth. Chem. Soc.*, 90:273-283, 1971.

A. Bohra, R. Bhatt, S. Bhattacharya, R. Basu, S. Ahmad, A. Singh, D. K. Aswal and S. K. Gupta. Study of thermal stability of Cu_2Se thermoelectric material. *AIP Conference Proceedings*, 1731:110010, 2016.

A. F. May, E. S. Toberer, A. Saramat and G. J. Snyder. Characterization and analysis of thermoelectric transport in n-type $\text{Ba}_8\text{Ga}_{16-x}\text{Ge}_{30+x}$. *Phys. Rev. B*, 80: 125205, 2009.

A. S. Nissimagoudar, N. S. Sankeshwar. Significant reduction of lattice thermal conductivity due to phonon confinement in graphene nanoribbons, *Phys. Rev. B*, 89:235422, 2014.

A. J. Hong, L. Li, H. X. Zhu, X. H. Zhou, Q. Y. He, W. S. Liu, Z. B. Yan, J. M. Liu and Z. F. Ren. Anomalous transport and thermoelectric performances of CuAgSe compounds, *Solid State Ion.*, 261:21-25, 2014.

B. Yu, W. S. Liu, S. Chen, H. Wang, H. Z. Wang, G. Chen and Z. F. Ren. Thermoelectric properties of copper selenide with ordered selenium layer and disordered copper layer, *Nano Energy*, 1:472-478, 2012.

- C. P. Liu, M. W. Chang and C. L. Chuang, The effect of Ga₂Se₃ doping ratios on structure, composition, and electrical properties of CuIn_{0.5}Ga_{0.5}Se₂ absorber formed by thermal sintering. *Int. J. Photoenergy*, 2013:936364-1-6, 2013.
- C. Xiao, J. Xu, K. Li, J. Feng, J. Yang, and Y. Xie. Superionic phase transition in silver chalcogenide nanocrystals realizing optimized thermoelectric performance. *J. Am. Chem. Soc.*, 134:4287- 4293, 2012.
- D. T. Morelli, V. Jovovic and J. P. Heremans. Intrinsically minimal thermal conductivity in cubic I-V-VI₂ semiconductors. *Phys. Rev. Lett.*, 101:035901, 2008.
- D. R. Brown, T. Day, T. Caillat and G. J. Snyder. Chemical stability of (Ag, Cu)₂Se: a historical overview, *J. Electron. Mater.*, 42:2014-2019, 2013.
- D. J. Voneshen, H. C. Walker, K. Refson and J. P. Goff. Hopping time scales and the phonon-liquid electron-crystal picture in thermoelectric copper selenide. *Phys. Rev. Lett.*, 118:145901, 2017.
- D. Wu, L. Zhao, X. Tong, W. Li, L. Wu, Q. Tan, Y. Pei, L. Huang, J. Li, Y. Zhu, M. G. Kanatzidis and J. He. Superior thermoelectric performance in PbTe-PbS pseudo-binary: extremely low thermal conductivity and modulated carrier concentration, *Energy Environ. Sci.*, 8:2056, 2015.
- D. M. Rowe. Thermoelectrics and its energy harvesting materials, preparation and characterization in thermoelectrics. *CRC Press Taylor & Francis Group*, 2012.
- D. Suh, D. Lee, C. Kang, I. J. Shon, W. Kim and S. Baik. Enhanced thermoelectric properties of tungsten disulfide-multiwalled carbon nanotube composites. *J. Mater. Chem.*, 22: 21376-21381, 2012.

- D. Guérard, R. Janot, Structure of the superdense LiC_3 compound prepared by ball-milling. *J. Phys. Chem. Solids*, 65:147-152, 2004.
- E. Li, S. Wang, Z. Zhu, R. Cao, X. Hu and H. Song. Enhanced thermoelectric properties of Hg-doped Cu_2Se . *Int. J. Mod. Phys. B*, 32:1850087, 2018.
- F. Hergert, S. Jost, R. Hock and M. Purwins. A crystallographic description of experimentally identified formation reactions of $\text{Cu}(\text{In, Ga})\text{Se}_2$. *J. Solid State Chem.*, 179:2394-2415, 2006.
- F. S. Liu, M. J. Huang, Z. N. Gong, W. Q. Ao, Y. Li and J. Q. Li. Enhancing the thermoelectric performance of $\beta\text{-Cu}_2\text{Se}$ by incorporating SnSe . *J. Alloy. Compd.*, 651:648-654, 2015.
- F. Gao, X. Du, F. Wu, X. Li, X. Hu and H. Song. Thermoelectric properties of $\text{Cu}_2\text{Se}/x\text{Ni}_{0.85}\text{Se}$ hot-pressed from hydrothermal synthesis nanopowders. *Mod. Phys. Lett. B*, 31:1750093 1-11, 2017.
- F. S. Liu, Z. N. Gong, M. J. Huang, W. Q. Ao, Y. Li and J. Q. Li. Enhanced thermoelectric properties of $\beta\text{-Cu}_2\text{Se}$ by incorporating CuGaSe_2 . *J. Alloy. Compd.*, 688:521-526, 2016.
- G. J. Snyder, E. S. Toberer. Complex thermoelectric materials, *Nat. Mater.*, 7:105-114, 2008.
- G. Stapfer, L. Garvey. Progress report No. 29 for a program of thermoelectric generator testing and RTG degradation mechanisms evaluation (Reprot no.DOE/ET/33003-T2) (DOE, 1979)
- G. Dennler, R. Chmielowski, S. Jacob, F. Capet, P. Roussel, S. Zastrow, K. Nielsch, I. Opahle and G. K. H. Madsen. Are binary copper sulfides/selenides really new and promising thermoelectric materials? *Adv. Energy Mater.*, 4:1301581, 2014.
- G. K. Solanki, D. N. Gujarathi, M. P. Deshpande, D. Lakshminarayana and M. K. Agarwal. Transport property measurements in tungsten sulphoselenide single crystals grown by a CVT technique. *Cryst. Res. Technol.* 43:179-185, 2008.

- F. Kaiser, P. Simon, U. Burkhardt, B. Kieback, Y. Grin and I. Veremchuk. Spark plasma sintering of tungsten oxides WO_x ($2.5 < x < 3$): phase analysis and thermoelectric properties. *Crystals*, 7:271-1-14, 2017.
- H. Guo, H. Xin, X. Qin, Z. Jian, D. Li, Y. Li and C. Li. Thermoelectric transport properties of PbTe-based composites incorporated with Cu_2Se nano-inclusions. *J. Phys. D- Appl. Phys.*, 49:065302, 2016.
- H. Chi, H. Kim, J. C. Thomas, G. Shi, K. Sun, M. Abeykoon, E. S. Bozin, X. Shi, Q. Li, X. Shi, E. Kioupakis, A. V. Ven, M. Kaviany and C. Uher. Low-temperature structural and transport anomalies in Cu_2Se . *Phys. Rev. B*, 89:195209, 2014.
- H. Kim, S. Ballikaya, H. Chi, J. P. Ahn, K. Ahn, C. Uher and M. Kaviany. Ultralow thermal conductivity of β - Cu_2Se by atomic fluidity and structure distortion. *Acta Mater.*, 86:247-253, 2015.
- H. Liu, X. Shi, M. Kirkham, H. Wang, Q. Li, C. Uher, W. Zhang and L. Chen. Structure-transformation-induced abnormal thermoelectric properties in semiconductor copper selenide. *Mater. Lett.*, 93:121-124, 2013.
- H. L. Liu, X. Yuan, P. Lu, X. Shi, F. F. Xu, Y. He, Y. S. Tang, S. Q. Bai, W. Q. Zhang, L. D. Chen, Y. Lin, L. Shi, H. Lin, X. Y. Gao, X. M. Zhang, H. Chi and C. Uher. Ultrahigh thermoelectric performance by electron and phonon critical scattering in $Cu_2Se_{1-x}I_x$, *Adv. Mater.*. 25:6607-6612, 2013.
- H. Liu, X. Shi, F. Xu, L. Zhang, W. Zhang, L. Chen, Q. Li, C. Uher, T. Day and G. J. Snyder. Copper ion liquid-like thermoelectrics, *Nat. Mater.*, 11:422-425, 2012.
- H. S. Lee. Thermoelectrics Design and materials. *John Wiley & Sons Ltd*, 2017.

- J. J. Kuo, S. D. Kang, K. Imasato, H. Tamaki, S. Ohno, T. Kanno and G. J. Snyder. Grain boundary dominated charge transport in Mg₃Sb₂-based compounds. *Energy Environ. Sci.*, 11:429-434, 2018.
- J. Y. Kim, J. C. Grossman. High-efficient thermoelectrics with functionalized graphene. *Nano lett.*, 15:2830-2835, 2015.
- J. D. Forster, J. J. Lynch, N. E. Coated, J. Liu, H. Jang, E. Zaia, M. P. Gordon, M. Szybowski, A. Sahu, D. G. Cahill and J. J. Urban. Solution-processed Cu₂Se nanocrystal films with bulk-like thermoelectric performance. *Sci. Rep.*, 7:2765, 2017.
- J. Y. Tak, W. H. Nam, C. H. Lee, S. Kim, Y. S. Lim, K. Ko, S. Lee, W. S. Seo, H. K. Cho, J. H. Shim and C. H. Park. Ultralow lattice thermal conductivity and significantly enhanced near-room-temperature thermoelectric figure of merit in α -Cu₂Se through suppressed Cu vacancy formation by overstoichiometric Cu addition. *Chem. Mat.*, 30:3276-3284, 2018.
- J. Zhang, X. Qin, D. Li, H. Xin, C. Song, L. Li, X. Zhu, Z. Wang, G. Guo and L. Wang. Enhanced thermoelectric performance of CuGaTe₂ based composites incorporated with nanophase Cu₂Se. *J. Mater. Chem. A*, 2:2891-2895, 2014.
- J. A. Perez-Taborda, L. Vera, O. Caballero, E. O. Lopez, J. J. Romero, D. G. Stroppa, F. Briones and M. Martin-Gonzalez. Pulsed hybrid reactive magnetron sputtering for high zT Cu₂Se thermoelectric films. *Adv. Mater. Technol.*, 2:1700012, 2017.
- J. Wang, B. Liu, N. Miao, J. Zhou and Z. Sun. I-doped Cu₂Se nanocrystals for high-performance thermoelectric applications. *J. Alloy. Compd.*, 772:366-370, 2019.
- K. P. Zhao, A. B. Blichfeld, H. Y. Chen, Q. F. Song, T. S. Zhang, C. X. Zhu, D. Ren, R. Hanus, P. F. Qiu, B. B. Iversen, F. F. Xu, G. J. Snyder, X. Shi and L. D. Chen. Enhanced thermoelectric

performance through tuning bonding energy in $\text{Cu}_2\text{Se}_{1-x}\text{S}_x$ liquid-like materials. *Chem. Mat.*, 29: 6367-6377, 2017.

K. C. Lukas, W. S. Liu, G. Joshi, M. Zebarjadi, M. S. Dresselhaus, Z. F. Ren, G. Chen and C. P. Opeil. Experimental determination of the Lorenz number in $\text{Cu}_{0.01}\text{Bi}_2\text{Te}_{2.7}\text{Se}_{0.3}$ and $\text{Bi}_{0.88}\text{Sb}_{0.12}$. *Phys. Rev. B*, 85:20540, 2012.

K. Yamamoto, S. Kashida. X-ray study of the average structures of Cu_2Se and $\text{Cu}_{1.8}\text{S}$ in the room temperature and the high temperature phase. *J. Solid State Chem.*, 93:202-211, 1991.

K. Biswas, J. He, I. D. Blum, C. I. Wu, T. P. Hogan, D. N. Seidman, V. P. Dravid and M. G. Kanatzidis. High-performance bulk thermoelectrics with all-scale hierarchical architectures. *Nature*, 489:414-418, 2012.

L. Wu, X. Li, S. Wang, T. Zhang, J. Yang, W. Zhang, L. Chen and J. Yang. Resonant level-induced high thermoelectric response in indium-doped GeTe. *NPG Asia Materials*, 9:e343, 2017.

L. Yang, Z. Chen, G. Han, M. Hong, L. Huang and J. Zou. Te-doped Cu_2Se nanoplates with a high average thermoelectric figure of merit. *J. Mater. Chem. A*, 23:9213-9219, 2016.

L. Yang, Z. Chen, G. Han, M. Hong, Y. Zou and J. Zou. High-performance thermoelectric Cu_2Se nanoplates through nanostructure engineering. *Nano Energy*, 16:368-374, 2015.

L. Yang, Z. Chen, G. Han, M. Hong, J. Zou. Impacts of Cu deficiency on the thermoelectric properties of Cu_{2-x}Se nanoplates. *Acta Mater.*, 113:140-146, 2016.

L. Zhao, G. Tan, S. Hao, J. He, Y. Pei, H. Chi, H. Wang, S. Gong, H. Xu, V. P. Dravid, C. Uher, G. J. Snyder, C. Wolverton and M. G. Kanatzidis. Ultrahigh power factor and thermoelectric performance in hole-doped single-crystal SnSe, *Science*, 351:141-144, 2016.

- L. L. Zhao, X. L. Wang, J. Y. Wang, Z. X. Cheng, S. X. Dou, J. Wang and L. Q. Liu. Superior intrinsic thermoelectric performance with zT of 1.8 in single-crystal and melt-quenched highly dense Cu_{2-x}Se bulks. *Sci. Rep.*, 5:7671, 2015.
- L. Gulay, M. Daszkiewicz, O. Strok and A. Pietraszko. Crystal structure of Cu_2Se , *Chem. Met. Alloys*, 4:200-205, 2011.
- L. Wu, X. Su, Y. Yan, C. Uher and X. Tang. Ultra-fast one-step fabrication of Cu_2Se thermoelectric legs with Ni-Al electrodes by plasma-activated reactive sintering technique. *Adv. Eng. Mater.*, 7:1181-1188, 2016.
- M. Oliveria, R. K. McMullan and B. J. Wuensch. Single crystal neutron diffraction analysis of the cation distribution in the high-temperature phases $\alpha\text{-Cu}_{2-x}\text{S}$, $\alpha\text{-Cu}_{2-x}\text{Se}$, and $\alpha\text{-Ag}_2\text{Se}$. *Solid State Ion.*, 28:1332-1337, 1988.
- M. Wood, U. Aydemir, S. Ohno and G. J. Snyder. Observation of valence band crossing: the thermoelectric properties of $\text{CaZn}_2\text{Sb}_2\text{-CaMg}_2\text{Sb}_2$ solid solution. *J. Mater. Chem. A*, 6:9437-9444, 2018.
- M. Rull-Bravo, A. Moure, J. F. Fernandez and M. Martin-Gonzalez. Skutterudites as thermoelectric materials: revisited. *RSC Adv.*, 5:41653, 2015.
- M. Li, D. L. Cortie, J. Liu, D. Yu, S. M. K. N. Islam, L. Zhao, D. R. G. Mitchell, R. A. Mole, M. B. Cortie, S. Dou and X. Wang. Ultra-high thermoelectric performance in graphene incorporated Cu_2Se : Role of mismatching phonon modes. *Nano Energy*, 53:993-1002, 2018.
- M. C. Wingert, J. L. Zheng, S. Kwon and R. K. Chen. Thermal transport in amorphous materials: a review, *Semicond. Sci. Technol.*, 31:113003-1- 16, 2016.

- P. Lu, H. Liu, X. Yuan, F. Xu, X. Shi, K. Zhao, W. Qiu, W. Zhang and L. Chen. Multiformality and fluctuation of Cu ordering in Cu₂Se thermoelectric materials. *J. Mater. Chem. A*, 3:6901-6908, 2015.
- P. Qiu, T. Zhang, Y. Qiu, X. Shi and L. Chen. Sulfide bornite thermoelectric material: a natural mineral with ultralow thermal conductivity. *Energy Environ. Sci.*, 7:4000, 2014.
- P. Zhang, Y. Meng, Z. Liu, D. Li, T. Su, Q. Meng, Q. Mao, X. Pan, D. Chen and H. Zhao. Impact of interfacial resistance switching on thermoelectric effect of Nb-doped SrTiO₃ single crystalline. *J. Appl. Phys.*, 111:063702, 2012.
- P. Peng, Z. N. Gong, F. S. Liu, M. J. Huang, W. Q. Ao, Y. Li and J. Q. Li. Structure and thermoelectric performance of β -Cu₂Se doped with Fe, Ni, Mn, In, Zn or Sm. *Intermetallics*, 75:72-78, 2016.
- R. D. Heyding, R. M. Murray. Crystal-Structures of Cu_{1.8}Se, Cu₃Se₂, α - and γ -CuSe, CuSe₂, and CuSe₂ II. *Can. J. Chem.*, 54:841-848, 1976.
- R. Nunna, P. Qiu, M. Yin, H. Chen, R. Hanus, Q. Song, T. Zhang, M. Chou, M. T. Agne, J. He, G. J. Snyder, X. Shi and L. Chen. Ultrahigh thermoelectric performance in Cu₂Se-based hybrid materials with highly dispersed molecular CNTs. *Energy Environ. Sci.*, 10:1928, 2017.
- S. A. Danilkin, A. N. Skomorokhov, A. Hoser, H. Fuess, V. Rajevac and N. N. Bickulova, Crystal structure and lattice dynamics of superionic copper selenide Cu_{2- δ} Se. *J. Alloy. Compd.*, 361:57-61, 2003.
- S. A. Danilkin, M. Avdeev, T. Sakuma, R. Macquart, C. D. Ling, M. Rusina and Z. Izaola. Neutron scattering study of short-range correlations and ionic diffusion in copper selenide. *Ionics*, 17: 75-80, 2011.

- S. Ballikaya, H. Chi, J. R. Salvador and C. Uher. Thermoelectric properties of Ag-doped Cu₂Se and Cu₂Te, *J. Mater. Chem. A*, 40:12478-12484, 2013.
- S. Cassaignon, S. Sanchez, J. F. Guillemoles, J. Vedel and H. G. Meier. Influence of the composition on the copper diffusion in copper sulfides study by impedance spectroscopy. *J. Electrochem. Soc.*, 146:4666-4671, 1999.
- S. N. Girard, J. He, X. Zhou, D. Shoemaker, C. M. Jaworski, C. Uher, V. P. Dravid, J. P. Heremans and M. G. Kanatzidis, High-performance Na-doped PbTe-PbS thermoelectric materials: electronic density of states modification and shape-Ccontrolled nanostructures, *J. Am. Chem. Soc.*, 133:16588-16597, 2011.
- S. Ballikaya, H. Chi, J. R. Salvador and C. Uher. Thermoelectric properties of Ag-doped Cu₂Se and Cu₂Te. *J. Mater. Chem. A*, 40:12478, 2013.
- S. Miyatani. Electronic and ionic conduction in (Ag_xCu_{1-x})Se, *J. Phys. Soc. Jpn.*, 34:423-432, 1973.
- S. D. Kang, J. Pöhls, U. Aydemir, P. Qiu, C. C. Stoumpos, R. Hanus, M. A. White, X. Shi, L. Chen, M. G. Kanatzidis and G. J. Snyder. Enhanced stability and thermoelectric figure-of-merit in copper selenide by lithium doping. *Materials Today Physics*, 1:7 -13, 2017.
- S. Namsani, S. Auluck and J. K. Singh, Thermal conductivity of thermoelectric material β -Cu₂Se: implications on phonon thermal transport. *Appl. Phys. Lett.*, 111:163903-1-5, 2017.
- S. Y. Miyatani, Y. Suzuki. On the electric conductivity of cuprous sulfide: experiment. *J. Phys. Soc. Jpn.*, 8:680-681, 1953.
- T. W. Day, K. A. Borup, T. Zhang, F. Drymiotis, D. R. Brown, X. Shi, L. Chen, B. B. Iversen and G. J. Snyder. High-temperature thermoelectric properties of Cu_{1.97}Ag_{0.03}Se_{1+y}, *Material for Renewable and Sustainable Energy*, 3:26, 2014.

T. P. Bailey, S. Hui, H. Xie, A. Olvera, P. F. P. Poudeu, X. Tang and C. Uher. Enhanced zT and attempts to chemically stabilize Cu_2Se via Sn doping. *J. Mater. Chem. A*, 4: 17225, 2016.

U. Aydemir, J. H. Pöhls, H. Zhu, G. Hautier, S. Bajaj, Z. M. Gibbs, W. Chen, G. D. Li, S. Ohno, D. Broberg, S. D. Kang, M. Asta, G. Ceder, M. A. White, K. Persson, A. Jain and G. J. Snyder. YCuTe_2 : a member of a new class of thermoelectric materials with CuTe_4 -based layered structure. *J. Mater. Chem. A*, 7:2461-2472, 2016.

X. Zhang, L. D. Zhao. Thermoelectric materials: Energy conversion between heat and electricity. *Journal of Materiomics*, 1:92-105, 2015.

Y. Z. Pei, H. Wang and G. J. Snyder, Band engineering of thermoelectric materials. *Adv. Mater.*, 24:6125-6135, 2012.

Y. X. Sun, L. L. Xi, J. Yang, L. H. Wu, X. Shi, L. D. Chen, J. Snyder, J. H. Yang and W. Q. Zhang. The “electron crystal” behaviour in copper chalcogenides Cu_2X ($\text{X}=\text{Se}, \text{S}$). *J. Mater. Chem. A*, 5:5098-5105, 2017.

Y. Y. Li, X. Y. Qin, D. Li, J. Zhang, C. Li, Y. F. Liu, C. J. Song, H. X. Xin, and H. F. Guo. Enhanced thermoelectric performance of $\text{Cu}_2\text{Se}/\text{Bi}_{0.4}\text{Sb}_{1.6}\text{Te}_3$ nanocomposites at elevated temperatures. *Appl. Phys. Lett.*, 108:062104, 2016.

Y. Zhu, B. Zhang and Y. Liu. Enhancing thermoelectric performance of Cu_2Se by doping Te. *Phys. Chem. Chem. Phys.*, 19:27664-27669, 2017.

Y. Pei, X. Shi, A. LaLonde, H. Wang, L. Chen and J. Snyder. Convergence of electronic bands for high performance bulk thermoelectrics. *Nature*, 473:66-69, 2011.

Z. Ge, B. Zhang, Y. Chen, Z. Yu, Y. Liu and J. Li. Synthesis and transport property of $\text{Cu}_{1.8}\text{S}$ as a promising thermoelectric compound. *Chem. Commun.*, 47:12697-12699, 2011.

Z. Peng, D. He, X. Mu, H. Zhou, C. Li, S. Ma, P. Ji, W. Hou, P. Wei, W. Zhu, X. Nie and W. Zhao.
Preparation and enhanced thermoelectric performance of Cu₂Se-SnSe composite materials. *J. Electron. Mater.*, 47:3350-3357, 2018.

<http://pd.chem.ucl.ac.uk/pdnn/peaks/sizedet.htm>